

Sensitivity and Distortion Studies of Positron Emission Tracking System

(PeTrack)

by

Simin Razavi

A Thesis submitted to

The Faculty of Graduate & Post Doctoral Affairs

in partial fulfilment of

the requirements for the degree of

Master of Science

in

Medical Physics

Ottawa-Carleton Institute of Physics

Department of Physics

Carleton University

Ottawa, Ontario, Canada

July 2014

Copyright ©

2014- Simin Razavi

Abstract

Positron Emission Tracking (PeTrack) is a new real-time 3D tracking technique. The project studied the sensitivity and distortion of the PeTrack system with four different detector field of view (FOV) configurations using Monte-Carlo simulation software (GATE). The simulation studies demonstrated the clear boundaries for FOV and also revealed a local distortion up to 1 mm for PeTrack. The simulation also showed that the detector misalignment could introduce the distortion to the system. The amplitude of the distortion is approximately the half of the misalignment at the center of the FOV. The results of simulations lead us to calibrate the PeTrack system to obtain the global scaling factors. However, since PeTrack has a non-uniform distortion across FOV, the global scaling factors were helpful to only some extent. The value of calculated average error after global scaling correction is less than 1 mm. The PeTrack system is also co-registered with an x-ray imaging C-arm to evaluate the tracking performance.

I would like to dedicate this thesis to

My true love Ahad,

My supportive family, &

My great supervisor, Dr. Tong Xu

Acknowledgment

I would like to thank those collaborators who made this project possible:

Dr. Tong Xu, my supervisor for his efforts and excellent guidances throughout this project,

Marc Chamberland, my colleague for the development of PeTrak algorithm and GATE simulation data,

Benjamin Spencer, my colleague for the co-registration of x-ray and C-arm.

Statement of Originality

The work presented here contains contributions of other graduate students other than myself and my supervisor Dr. Tong Xu.

I am the first to investigate the distortion and sensitivity of PeTrack system. I am also the first to study the effects of misalignment on the PeTrack system. The PeTrack simulation model is originally established in GATE by Marc Chamberland. I modified the simulation model to introduce different detector configurations and misalignments for this study. The tracking algorithm is written by Marc Chamberland and I used it for all of the experiments on PeTrack system. The calibration of PeTrack is done by myself and I used the global calibration scaling factors to improve the results of the tracking. I performed co-registration between PeTrack and x-ray C-arm using the co-registration method and the software developed by Benjamin Spencer.

Table of Content

Chapter 1	Introduction to PeTrack System	
1.1	Overview.....	1
1.2	Methods of Real-Time Tracking in Medicine.....	1
1.2.1	Fluoroscopy.....	2
1.2.2	Electromagnetic (EM) Tracking.....	2
1.2.3	MRI.....	2
1.2.4	Ultrasound.....	3
1.3	PeTrack.....	3
1.3.1	Positron Decay	6
1.3.2	Structure of PeTrack.....	8
1.3.3	Geometry.....	9
1.3.4	Algorithm.....	10
1.3.4.1	Single Marker Tracking Algorithm.....	11
1.3.4.2	Multi-Marker Tracking Algorithm.....	11

1.3.5	Sensitivity.....	15
1.3.6	Distortion.....	16
1.4	Summary.....	17
Chapter 2	Field of View and Simulation Studies	
2.1	Overview.....	18
2.2	Field of View, FOV.....	18
2.3	Monte Carlo Simulation in GATE.....	21
2.3.1	Structure of GATE.....	21
2.3.2	Features of GATE.....	22
2.4	Assembling the Simulation Elements.....	22
2.4.1	Detector.....	24
2.4.2	Physics.....	25
2.4.3	Digitizer.....	25
2.4.4	Source.....	25
2.4.5	Capsule.....	25
2.5	Selection of Different Detector Configurations.....	25
2.5.1	Simulation Data Processing.....	26

2.6	Results of Different Detector Configurations.....	26
2.6.1	Sensitivity and Error Maps of Configuration A.....	26
2.6.2	Sensitivity and Error Map of Configuration B.....	29
2.6.3	Sensitivity and Error Map of Configuration C.....	31
2.7	Simulation of PeTrack Prototype.....	32
2.7.1	Results of the Prototype PeTrack.....	34
2.8	Graphical Interpretation of the Results.....	39
2.9	Discussion.....	40
2.10	Summary.....	40
Chapter 3	The Effects of Misalignment	
3.1	Overview.....	42
3.2	Misalignment.....	42
3.2.1	Introducing a Misalignment.....	43
3.3	Results of Misalignment in X Direction.....	44
3.4	Results of Misalignment in Y Direction.....	47
3.5	Discussion.....	49

Chapter 4	Calibration of PeTrack System	
4.1	Overview.....	51
4.2	Set-up of the Calibration Experiment.....	51
4.2.1	Calibration in Both Direction	52
4.3	Data Analysis.....	53
4.3.1	Calculations.....	54
4.4	Results.....	55
4.5	Repeatability.....	57
4.6	Discussion.....	58
Chapter 5	Sensitivity and Distortion Survey of the Prototype PeTrack System	
5.1	Overview.....	60
5.2	Instrumentation and Method.....	61
5.3	Results.....	62
5.4	Discussion.....	66
Chapter 6	Integrate of PeTrack with X-ray System	
6.1	Overview.....	67

6.2	Dual x-ray/ PeTrack Calibration Phantom.....	67
6.3	Co-registration.....	68
6.4	A Moving Source inside a Tube.....	71
6.5	Results.....	71
6.6	Discussion.....	71

Chapter 7 Integrate of PeTrack with x-ray system

7.1	Simulation Studies.....	72
7.2	Sensitivity.....	72
7.3	Distortion.....	73
7.4	Future Work.....	73

List of Tables

4.1: Part of the calibration data on x-z and x-y planes.....	53
4.2: The results of the fitting for x-y and x-z planes	55
4.3: Comparison of applying scaled factor on deviation between experimental and grid data	57
4.4: Part of the repeatability data	58
5.1: The PeTrack measured pitches in x-y plotter experiment.....	63
6.1: The original and tracked source location on dual phantom.....	70

List of Figures

1.1: PeTrack system with a phantom in its center.....	3
1.2: A PeTrack marker	4
1.3: The process of the detecting of the marker by PeTrack.....	5
1.4: One of the applications of PeTrack in cardiac catheterization	6
1.5: The positron range	7
1.6: Non-collinearity of positron annihilation	8
1.7: A PeTrack detector modules	9
1.8: An array of BGO crystal	9
1.9: The geometry of PeTrack	9
1.10: (a) A true coincidence, (b) a scattered coincidence, (c) a random coincidence	10
1.11: The estimated location of the marker and its distances to the COILS.....	13
1.12: The solid angle of the detector for an annihilation at the isocenter of PeTrack	15
1.13: The solid angle of the detector for an annihilation at the edge of the PeTracks' FOV.....	16
2.1: The detector module of PeTrack with crystal IDs	19

2.2: Single Module Detector and different detector configurations	21
2.3: The raster motion	23
2.4: The PeTrack geometry	23
2.5: Simulated PeTrack system in GATE	24
2.6: The sensitivity map of configuration A	27
2.7: The error map of configuration A	28
2.8: The sensitivity map of configuration B	29
2.9: The error map of configuration B	30
2.10: The sensitivity map of detector C	31
2.11: The error map of detector C	32
2.12: The Prototype PeTrack geometry with the raster motion of the source on the planes.....	33
2.13: The sensitivity map of prototype detector	34
2.14: The error map of prototype detector in 3D	35
2.15: The error map of prototype detector in z direction	36
2.16: The error map of prototype detector in y direction	37
2.17: The error map of prototype detector in x direction	38
2.18: Comparison between two detector blocks with and without gap between them	39

3.1: Introducing a misalignment by shifting crystals	43
3.2: Shifting the crystals in x direction (i-shift) and y direction (j-shift).....	44
3.3: Sensitivity map after applying gap in x direction	45
3.4: The error map after applying gap in x direction.....	46
3.5: Sensitivity map after applying gap in y direction	47
3.6: The error map after applying gap in y direction	48
3.7: The FOV of detector modules along main axes	49
4.1: Calibration on X-Z plane	53
4.2: Calibration on X-Y plane	53
4.3: The result of experimental and grid data on X-Z	
(a) Non-scaled data (b) Scaled data	55
4.4: The result of experimental and grid data on X-Y	
(a) Non-scaled data (b) Scaled data.....	56
5.1: Tracking a moving source on x-y plotter	62
5.2: The tracked and true locations on x-y and x-z.....	63
5.3: The deviation of tracked and true locations on x-y	64
5.4: The deviation of tracked and true locations on x-z.....	64

5.5: Sensitivity map on x-y	64
5.6: Sensitivity map on x-z	64
5.7: Sensitivity map of simulated prototype on x-y	65
6.1: The dual phantom of PeTrack	68
6.2: An X-ray image of dual phantom of PeTrack	70
6.3: The image shows the path of the positron source inside the tube	71

List of Abbreviations

2D	Two dimensional
3D	Three dimensional
α_k	Relative activity of marker k
β^+, e^+	Positron
γ	photon (gamma ray)
ν	Neutrino
σ_k	Standard deviation of the distribution of the minimum distance between a marker k and its coincidence lines
σ_m	Precision of the localization of a marker
BGO	Bismuth germinate ($\text{Bi}_4\text{Ge}_3\text{O}_{12}$)
CT	Computed tomography
$\vec{d}(\mathbf{L}_n, \vec{m}_k)$	Minimum distance vector from coincidence line L_n to marker m_k
EM	Electromagnetic
EM T	Electromagnetic tracking
FOV	Field of view
FWHM	Full width half maximum
$G(\vec{d}(\mathbf{L}_n, \vec{m}_k) \sigma_k)$	Probability density function of the Gaussian distribution of the minimum distance between a marker and its coincidence lines
i	iteration index

k	Marker index
K	Total number of markers
L_n	Coincidence line n
m_k	Location of marker k
LINAC	Linear accelerator
MIR	Magnetic resonance imaging
PET	Positron emission tomography
PeTrack	Positron emission real-time tracking
PMT	Photo-multiplier tube
SPECT	Single photon emission computed tomography
US	Ultrasound

Chapter 1

Introduction to PeTrack System

1.1 Overview

This chapter focuses on the current methods of real-time tracking in medicine and introduces PeTrack as a novel 3D real-time tracking technique. Moreover, PeTrack system is discussed in terms of components, basic physics, geometry and the algorithm. In addition, sensitivity and distortion as two main characteristics of PeTrack are introduced.

1.2 Methods of Real-Time Tracking in Medicine

Image-guided surgery and real-time tracking are now used in patient care to overcome limitations of traditional open and invasive medical procedures. There are several methods to obtain information about the size, position, and orientation of the internal organs and surgical instruments such as fluoroscopy imaging, MRI, electromagnetic inducers, and ultrasound.

1.2.1 Fluoroscopy

Fluoroscopy is an imaging technique based on x-rays. In a recent research x-ray fluoroscopically-guided cardiac electrophysiology (EP) is performed for the reason of diagnosing and treatment of cardiac arrhythmias. The accuracy of the mentioned method is sub-millimetre and it is usable in low dose x-ray fluoroscopic image [1]. In radiotherapy, Fluoroscopy is used for real-time tumour tracking in order to deliver a precise dosage to the malignant tissues. Markers need to be implanted into the tumour for real-time image-guided radiotherapy. Although Fluoroscopy is beneficial in terms of high temporal resolution, it involves radiation that is a risk to the patient and operator [2].

1.2.2 Electromagnetic Tracking (EMT)

Electromagnetic method tracking relies on a changing (AC) or quasi static (DC) magnetic field induction. Electromagnetic Tracking, EMT, utilizes a magnetic field of a known geometry to determine the position of sensors for measuring magnetic flux. EMT has been in use for a number of medical applications including image-guided interventional therapy and surgery, endoscopic navigation, and more recently, positioning and tracking systems for prostate radiotherapy. In clinical applications the accuracy of EMT can be affected by magnetic field distortion due to other ferromagnetic objects and other imaging devices. Furthermore, it is inconvenient for patients to keep all of the hardware components such as field generator and EM sensors close or attached to them. These are considered as drawbacks for EMT [3, 4].

1.2.3 MRI

Magnetic resonance imaging is a non-ionizing method for real-time motion monitoring that gives a high contrast volumetric image of soft tissues. Current MRI technology has to be improved to

reach a high spatial and temporal resolution of real-time acquisition and reconstruction of the respiratory motion [5]. The problem with MRI is that it is costly.

1.2.4 Ultrasound

Ultrasound (US) is a non-ionizing and promising method in imaging. US has been in use for real-time monitoring of radiotherapy to deliver the dose precisely to the tumour while minimizing the dose to surrounding healthy tissues. US is a perfect modality for real-time imaging of soft tissue, such as the prostat. US imaging for tracking suffers from a limited ability to form an image of the instrument in the vicinity of some tissues such as bone and lung [6].

1.3 PeTrack

PeTrack (Positron Emission Tracking) is a new technique introduced by Dr. Tong Xu et al [7]. The PeTrack system consists of two pairs of position sensitive gamma ray detectors. The structure and alignment of PeTrack system is illustrated in Figure 1.1.

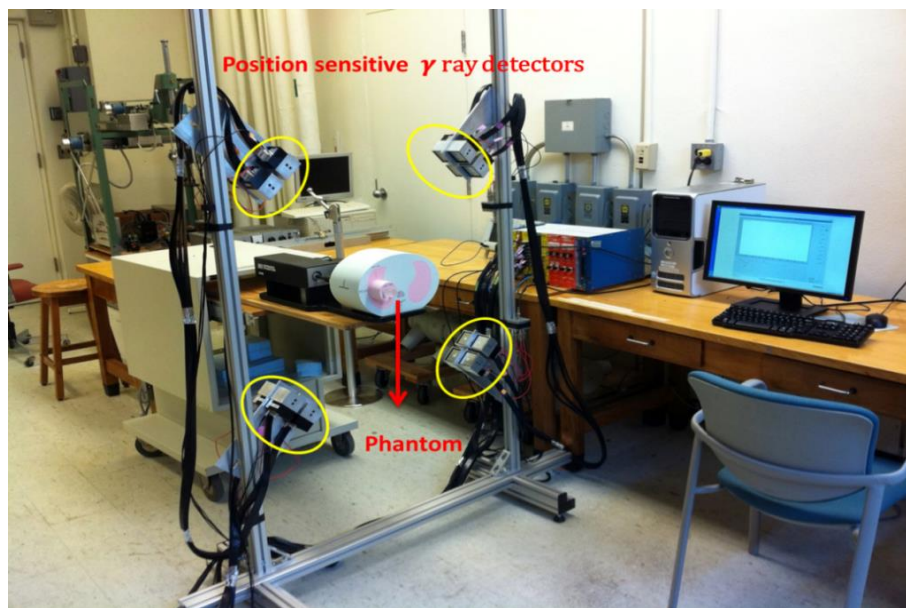


Figure 1.1: PeTrack system with a phantom in its centre.

A phantom is placed at the isocentre of the PeTrack and a positron emitter marker is attached to the target to be tracked inside the phantom. Each PeTrack marker contains a point source of positron emitting isotope (Figure 1.2). PeTrack has been designed to track the location of positron emitting markers, either implanted in patient's organ or attached to intervention tools. The activity is very low (0.03-0.2 mCi) which results in a small amount of radiation in the patient and the operator [7]. Single or multiple markers need to be attached to the target of interest to be tracked by PeTrack.

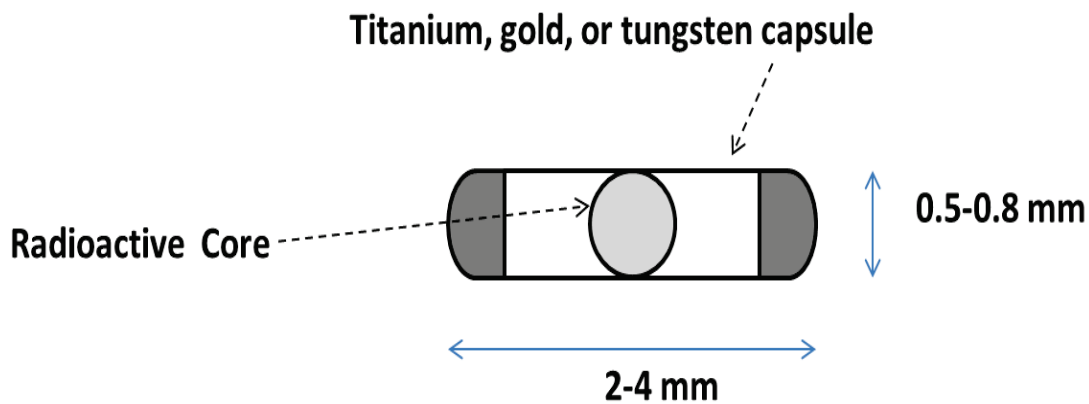


Figure 1.2: A PeTrack marker [7].

The emitted positron annihilates with an electron producing two gamma rays which are traveling away from each other in opposite directions (180°). The gamma rays hit the pixelated scintillation crystals. The scintillation crystals are coupled to position sensitive photo multiplier tubes (PMTs) which record the location of the hit on the crystals. The data are transferred to the read out system to assure that the detected gamma rays belong to single annihilation i.e. in coincidence. When two gamma rays hit the detectors they form a co-incidence line. The data are transferred to a computer to analyze and to determine the location of the marker in 3D (Figure 1.3). Certainly, the accuracy of PeTrack in detecting the location of the marker is crucial. Indeed the goal of this project is to study the sensitivity and distortion of PeTrack system.

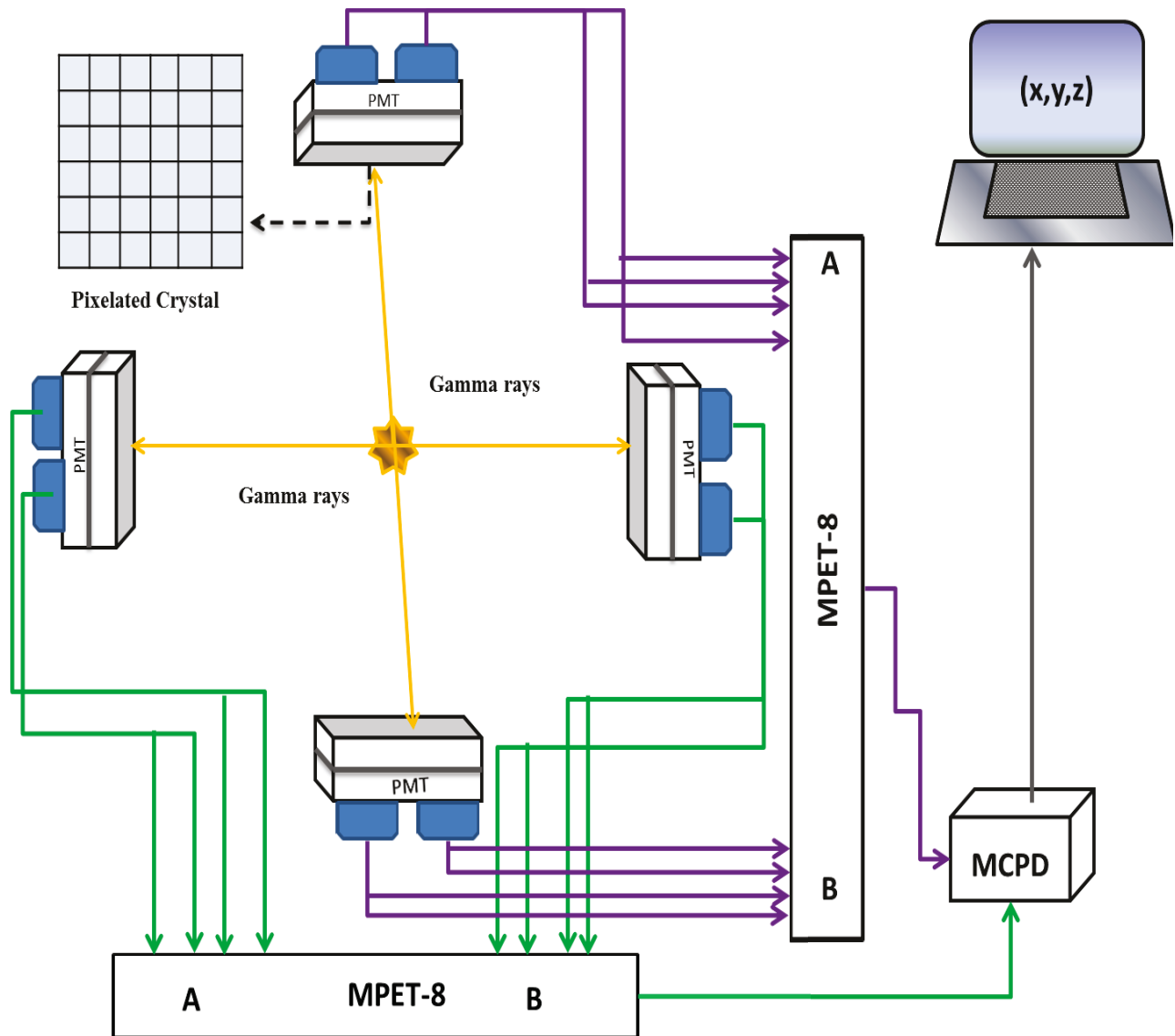


Figure 1.3: Schematically shows the process of annihilation, detector crystal hit by gamma rays, determining the location of hit by PMTs, transferring the data to readout system and finally detecting the 3D locations of the marker [8]. Two yellow lines are the co-incidence lines which are the result of two annihilation events. The yellow star indicates the location of the marker which is at the intersection of two co-incidence lines.

One of the applications of PeTrack is in image-guided surgery. As mentioned before the PeTrack marker can be attached to the intervention tools such as catheter. While catheter is moving in the interior organs, PeTrack system is able to report the location of the catheter during operation. Figure 1.4 shows one of the applications of PeTrack in cardiac catheterization.

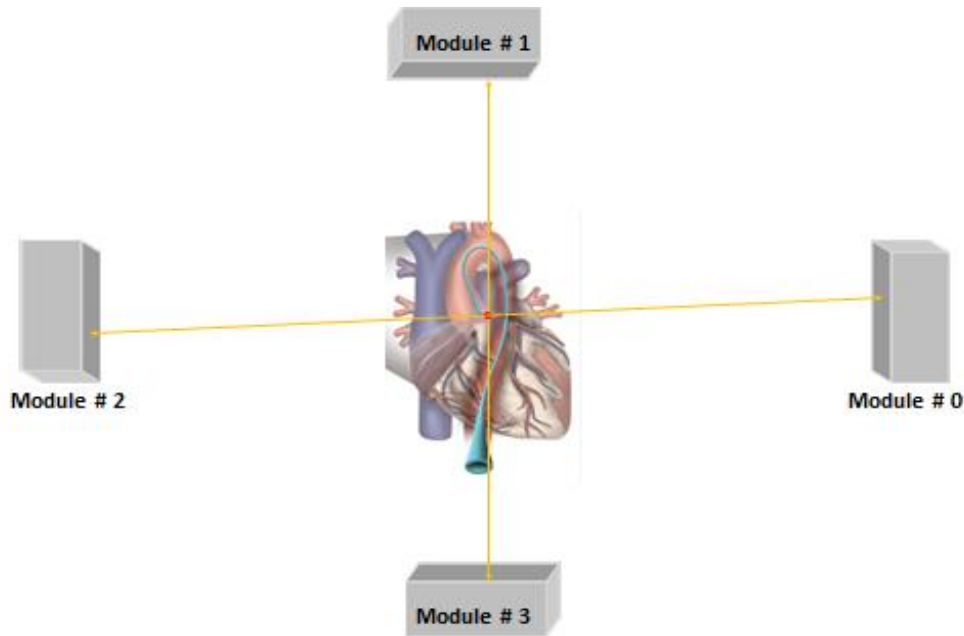


Figure 1.4: One of the applications of PeTrack is the tracking of the catheter. A PeTrack marker is attached to the tip of the catheter.

1.3.1 Positron Decay

The PeTrack system relies on the detection of gamma rays resulting from positron annihilation. A Positron emitter isotope can be generated by bombarding a stable nucleus by protons produced by cyclotron to generate a proton-rich nucleus. A positron (e^+) is generated when a proton inside a proton-rich nucleus transforms into a neutron and ejects a positron and a neutrino [10]. Neutrino is an uncharged particle which has a negligible mass and positron is the anti-matter of the electron [9].



The interactions of electrons and positrons within a medium could be an inelastic collisions, bremsstrahlung emission, or annihilation. Annihilation results in the production of two 511 keV gamma rays which are traveling in opposite directions to conserve momentum [10].



If two annihilation gamma rays are detected by two position sensitive gamma ray detectors, the line along which the gamma rays have traveled can be reconstructed, which is called coincidence line. The point positron source is expected to be somewhere along this line. However this is not exactly true due to the following two reasons.

Positron range: The positrons emitted from the positron decay traveling through a medium lose their energy by ionizing and radiative collisions which result in significant deflection [10]. The range of a positron is defined as the distance of the medium that the positron can travel until it stops. The positron range depends on the kinetic energy of the positron, and the material that the positron is in [10]. Positron range is one of the most important factors in PeTrack resolution [11].

Figure 1.5 illustrates the positron range and its annihilation with an electron.

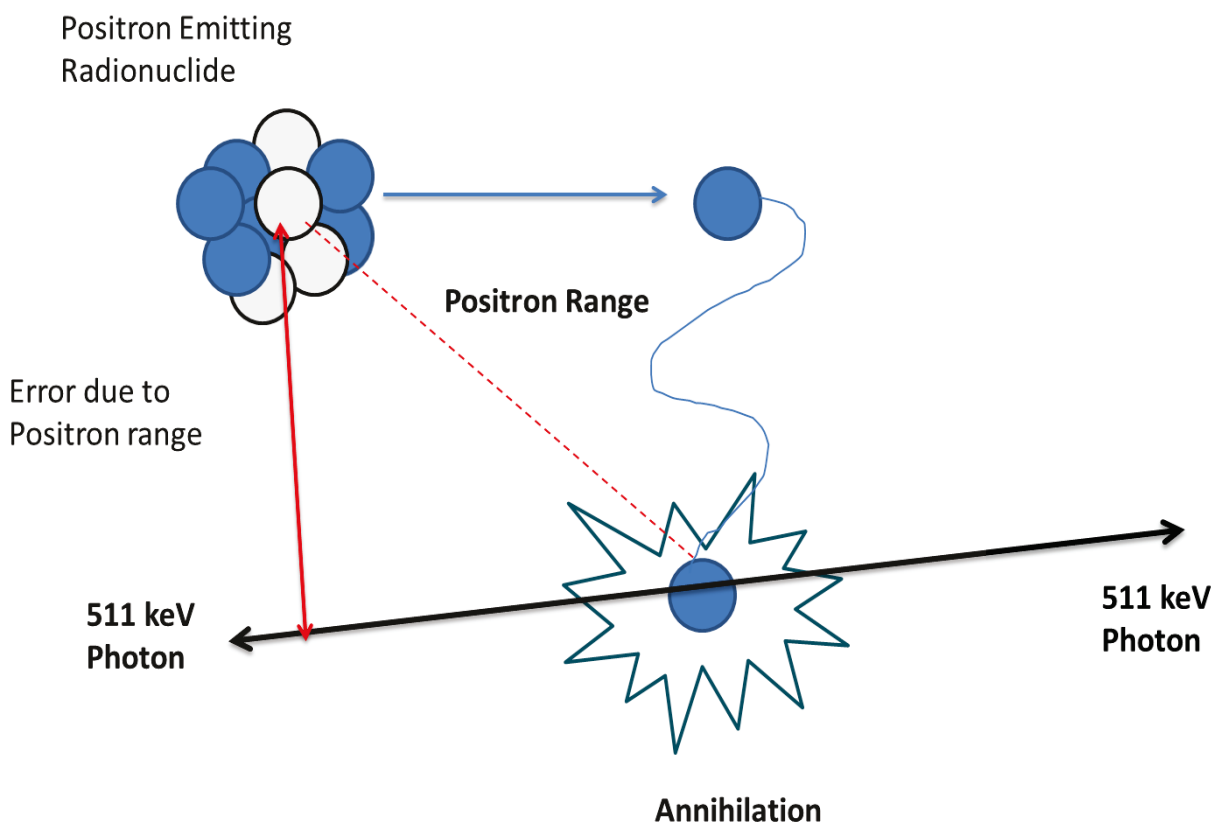


Figure 1.5: Positron range and its annihilation with an electron. The figure is not scaled [12].

Non-collinearity : When annihilation takes place the positron and electron are not at rest and both have a small net momentum which cause the annihilation photons do not be at the exactly 180 degrees but with a distribution of angles around 180°. The distribution of angle is almost a Gaussian in shape with a full-width-half-maximum (FWHM) of 0.5° [12]. The non-collinearity in the positron annihilation is shown in Figure 1.6 with an exaggeration.

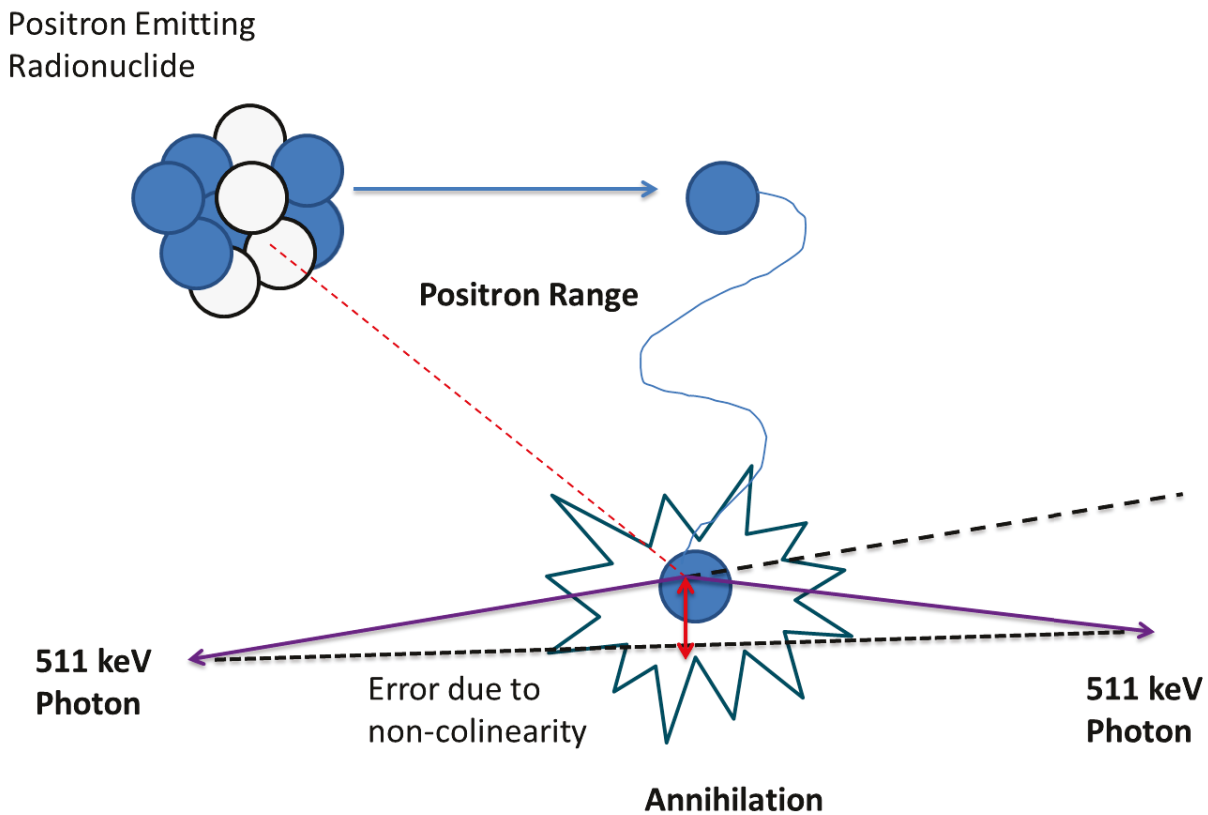


Figure 1.6: Non-collinearity of positron annihilation. The figure is not scaled [12].

1.3.2 Structure of PeTrack

PeTrack consists of four detector modules which each contains four detector blocks. Figure 1.7 depicts one of the detector modules in PeTrack system. In PeTrack detectors, Bismuth Germanate (BGO) crystal is used as the scintillator. BGO's chemical formula is $\text{Bi}_4\text{Ge}_3\text{O}_{12}$ and its effective atomic number is $\bar{Z} = 74$. It has a high density $\rho = 7.13 \text{ g/cm}^3$ which results in high

gamma ray absorption compared to NaI ($\bar{Z}= 50$ and $\rho = 3.67 \text{ g/cm}^3$). In BGO crystal 40 % of its interactions undergo to photoelectric effect. BGO crystals also demonstrate high radiation hardness and low afterglow [13]. Each detector block contains a 12×12 array of BGO crystal elements (Figure 1.8). Each crystal element has a $4 \times 4 \text{ mm}^2$ cross section area and a thickness of 2 cm. Each crystal array is coupled to a position sensitive photo-multiplier tube (H8500, Hamamatsu Co) with a sensitive area of $49 \times 49 \text{ mm}^2$ correspondent to the size of crystal array. Two gamma rays which are the results of the annihilation hit the scintillation crystal while causing excitation of its atoms. Some part of the released energy from de-excitation re-emits as visible light. The photo-multiplier collects the visible light and transforms it to the electrical signal [14].



Figure 1.7: A PeTrack detector module



Figure 1.8: An array of BGO crystal

1.3.3 Geometry

The detector geometry is displayed in Figure 1.9. The two pairs of PeTrack detector modules are placed in orthogonal directions: along y and z axes. The x axis is pointing into the page. This configuration of detectors allows the PeTrack to detect two coincident gamma rays traveling in opposite directions. The intrinsic spatial resolution of the detector is determined by the crystal element size, i.e. 4 mm.

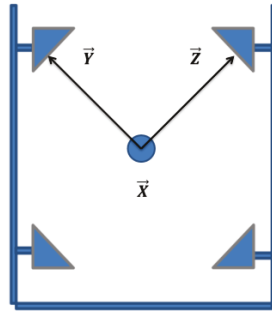


Figure 1.9: shows 4 detector modules indicated by triangle shapes. The detectors are attached to the supporting frame. The coordinate system used by PeTrack is shown by x, y, and z . The direction of x is into the page at the isocentre of PeTrack.

1.3.4 Algorithm

PeTrack algorithm relies on the detection of true coincidence events. In a true coincidence event, the two detected gamma rays are from single positron annihilation. Scatter coincidence arise when one of the annihilation photons undergoes a Compton scattering and its energy and direction are changed [12] (Figure 1.10).

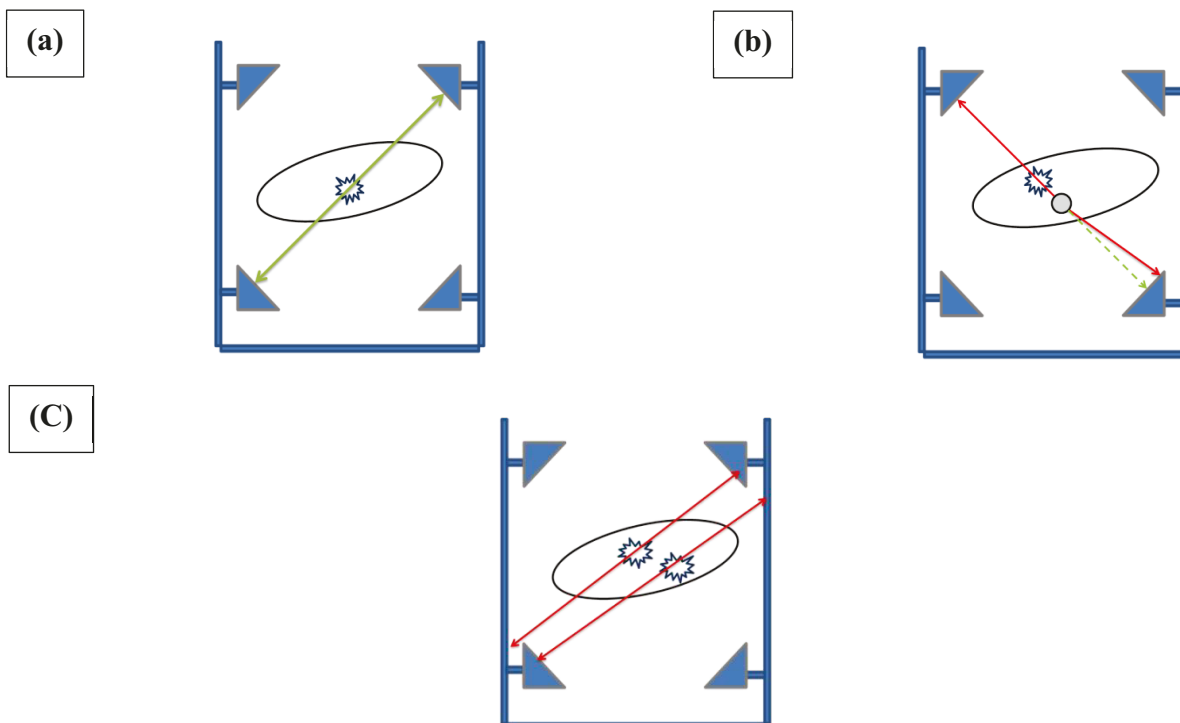


Figure 1.10: (a) A true coincidence, (b) A scattered coincidence, (c) A random coincidence [12].

On the other hand, when the detected gamma rays are not the result of the same annihilation, it is called a random coincidence as shown in Figure 1.10. In the PeTrack system a coincidence time window of 30 ns has been chosen to limit the detection of random coincidences. The temporal resolution of PeTrack system is 3.1 ns [8].

1.3.4.1 Single Marker Tracking Algorithm

The PeTrack system is able to track a single marker or multiple markers. In this project most of the experiments were done using a single marker. In the absence of scattering and non-collinearity positron source will annihilate with an electron emitting two perfect back-to-back gamma rays (511 keV). Two pairs of gamma rays that cross the centre of coincidence determine the location of the source. But, with the spatial uncertainty due to positron range, non-collinearity of annihilation gammas, and intrinsic resolution of detectors, the two coincident lines may not cross each other at all. In order to improve the localization, many pairs of annihilation gamma rays are required. The location of the source in 3D is where a collection of coincidence lines have the minimum distance from each other. The accuracy for localization is defined by σ/\sqrt{N} , where σ is the intrinsic spatial resolution of the system and N is the number of detected coincidence lines [7]. The intrinsic spatial resolution of PeTrack is determined by three factors as the following equation shows:

$$\sigma = \sqrt{\sigma_{\text{crystal}}^2 + \sigma_{\text{non-collinearity}}^2 + \sigma_{\text{positron range}}^2} \quad (1.3)$$

Where the σ_{crystal} is the intrinsic resolution of the crystal, $\sigma_{\text{non-collinearity}}$ is the error introduced by non-collinearity, and $\sigma_{\text{positron range}}$ is the error caused by positron range.

1.3.4.2 Multi-Marker Tracking Algorithm

The PeTrack system have been shown to be able to track up to $K=4$ markers [7, 15]. An expectation-maximization (EM) clustering algorithm is used to track the location of each of the K markers. Each marker has a marker index k which ranges from $k=1$ to K . In the multi-marker tracking algorithm it is assumed that the distance from the centre of a marker to its coincidence lines follow a Gaussian distribution. The Gaussian distribution has a mean of zero and a standard deviation of σ_k . The probability density function (PDF) for this Gaussian distribution is given by:

$$G(|\vec{d}(\mathbf{L}_n, \vec{m}_k)|\sigma_k) = \frac{1}{\sqrt{2\pi}\sigma_k} \exp\left(-\frac{|\vec{d}(\mathbf{L}_n, \vec{m}_k)|^2}{2\sigma_k^2}\right) \quad (1.4)$$

The PDF $G(|\vec{d}(\mathbf{L}_n, \vec{m}_k)|\sigma_k)$ is a one dimensional function of $\vec{d}(\mathbf{L}_n, \vec{m}_k)$ which is the minimum distance vector between the locations of an estimated marker (m_k) to one of the coincidence lines (\mathbf{L}_n) generated by the same marker [7].

The iterative part of the algorithm starts with an initial estimate of the location of the markers. This is done by the initialization algorithm, which first finds the centre of mass of the multiple markers. The initialization algorithm can be summarized in the following steps [15]:

1. Randomly select three coincidence lines from the set of events recorded in the first localization interval. For example, 300 coincidence lines are typically collected per localization for three markers.
2. Calculate the minimum distance between each pair of coincidence lines. If all three coincidence lines are not within 5 mm of each other, it is highly probable that they did not originate from the same marker. In this case, repeat step 1.
3. Calculate the three midpoints between each pair of coincidence lines.
4. Repeat steps 1 through 3, 3500 times.

5. Take the centre of mass of the 1500 midpoints obtained from steps 1 to 4.
6. Initialize the EM algorithm randomly around the centre of mass for each of K different markers.
7. After initializing the estimation of the marker locations, the main algorithm classifies the coincidence lines iteratively. Each iteration number i , starts with an estimation of the probability of each coincidence line L_n , ($n = 1, \dots, N$) belonging to a marker k is define as follows:

$$P_{n,k}^{(i)} = \frac{\alpha_k^{(i)} G \left(\left| \vec{d}(L_n, \vec{m}_k^{(i)}) \right|, \sigma_k^{(i)} \right)}{\sum_{j=1}^K \alpha_j^{(i)} G \left(\left| \vec{d}(L_n, \vec{m}_j^{(i)}) \right|, \sigma_j^{(i)} \right)} \quad (1.5)$$

In fact $P_{n,k}^{(i)}$ is the probability of each coincidence line L_n belonging to each marker k . Figure

1.11 shows the estimated location of marker (\mathbf{m}_k) and its distance to the co-incidence lines.

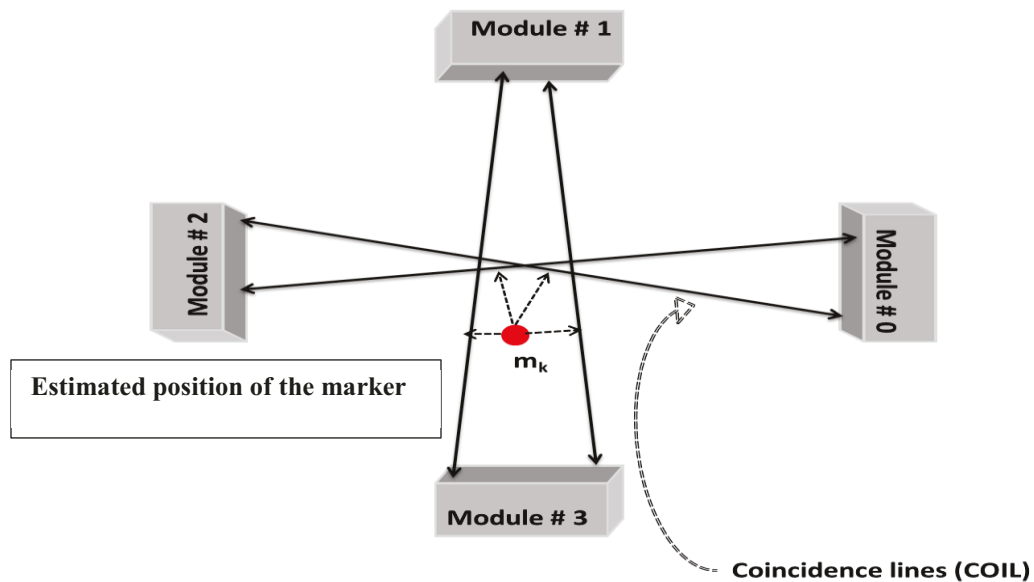


Figure 1.11: The estimated location of the marker and its distances to the COILs.

In equation (1.5) the relative activity of each marker, $\alpha_k^{(i)}$ and the standard deviation of the minimum distance between the coincidence lines and their corresponding markers, $\sigma_k^{(i)}$ are updated after each iteration, and the new parameters for the $(i+1)$ th iteration are:

$$\alpha_k^{(i+1)} = \frac{\sum_{n=1}^N p_{n,k}^{(i)}}{N} \quad (1.6)$$

$$\sigma_k^{(i+1)} = \sqrt{\frac{\sum_{n=1}^N p_{n,k}^{(i)} \cdot \left| \vec{d}(\mathbf{L}_n, \vec{m}_k^{(i)}) \right|^2}{\sum_{n=1}^N p_{n,k}^{(i)}}} \quad (1.7)$$

The next step of the iteration algorithm is the maximization step. A shift vector that reduces the RMS distance of a marker to its coincidence lines is defined as $\vec{d}(\mathbf{L}_n, \vec{m}_k^{(i)})$.

With each weight is given by equation (1.5), have:

$$\vec{V}_k^{(i)} = \frac{\sum_{n=1}^N p_{n,k}^{(i)} \cdot \vec{d}(\mathbf{L}_n, \vec{m}_k^{(i)})}{\sum_{n=1}^N p_{n,k}^{(i)}} \quad (1.8)$$

The new estimated position of the marker for the $(i+1)$ th iteration is:

$$\vec{m}_k^{(i+1)} = \vec{m}_k^{(i)} + \vec{V}_k^{(i)} \quad (1.9)$$

Not all coincidences that the algorithm uses are true coincidences. There will be random or scatter coincidences as well. In order to minimize the contribution of random and scatter coincidences, a condition is applied to the algorithm such that if the distance between the line \mathbf{L}_n and the estimated location of marker $\vec{m}_k^{(i)}$, $\vec{d}(\mathbf{L}_n, \vec{m}_k^{(i)}) > 2 \alpha_k^{(i)}$, the probability of coincidence line, \mathbf{L}_n belonging to cluster k is set to zero[7, 15].

1.3.5 Sensitivity

Sensitivity is the ability of the detector to detect the true coincidences. The sensitivity of PeTrack is defined as the number of the true coincidences per source activity that can be detected by the two pairs of detectors within a time interval of one second. Moreover, the sensitivity can vary significantly with the position of the PeTrack marker. In a better expression the spatial position of the marker determines the solid angle of which the true coincidence gammas can be detected by the detector pairs. Regarding the geometry of the PeTrack the solid angle in 3D has the shape of a pyramid which is illustrated in Figure 1.12. The mentioned figure illustrates the maximum solid angle when the annihilation happens at the isocentre and the most true coincidences can be detected by both detector pairs. This position has the highest sensitivity.

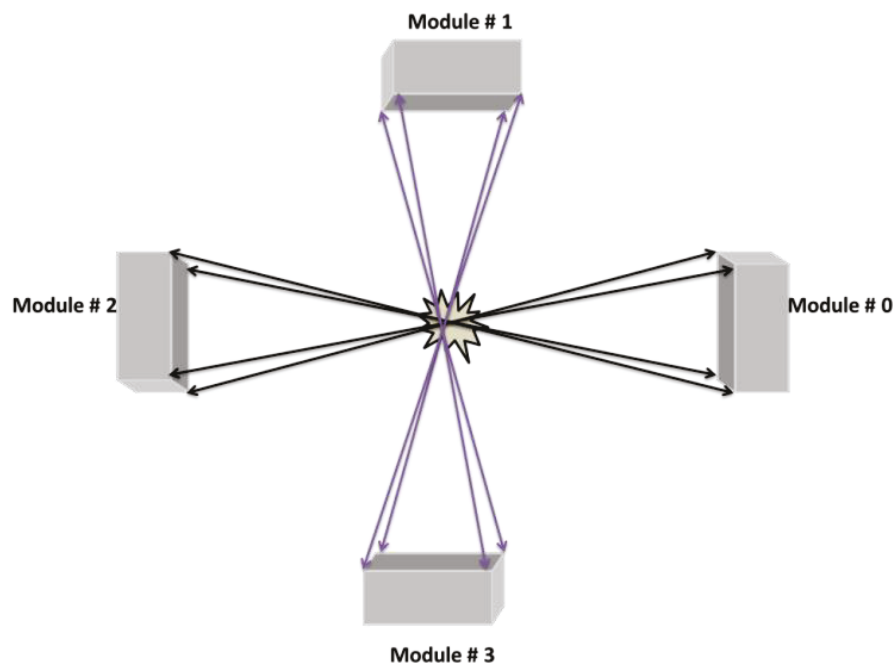


Figure 1.12: The solid angle of the detector for an annihilation at the isocentre of PeTrack.

On the other hand, when an annihilation takes place somewhere out of isocentre the solid angle diminish as shown at figure 1.13. One of the goals of this study is to map out the sensitivity distribution across the 3D field of view (FOV) of PeTrack system.

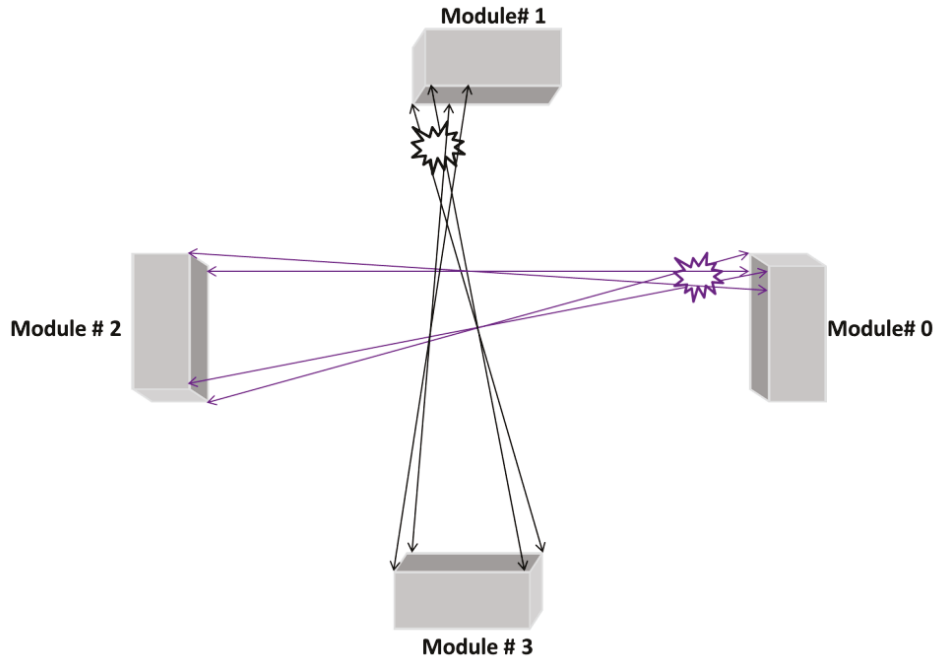


Figure 1.13: The solid angle of the detector for an annihilation at the edge of the PeTracks' FOV.

1.3.6 Distortion

Another goal of this project is to study the possible spatial distortions of PeTrack system. In PeTrack distortion could be introduced into the system by non-uniform sensitivity. When the solid angle of the detector is diminishing at the edge of the FOV, the number of true coincidences is decreasing and the PeTrack algorithm misidentifies the midpoint of the coincidence lines. As a result, PeTrack system fails to detect the exact location of the source. One of the solutions to reduce the mentioned degrading factor is to determine an efficient FOV, which is analysed in chapter 2. Distortion can be measured by a precise calibration test. It is possible also to correct the distortion if it is sufficiently constant and predictable between calibration test and data acquisition process [16].

1.4 Summary

This chapter introduced the motivation of establishing the PeTrack system as a real-time tracking technology. Overall the hardware and software of PeTrack system are discussed. The basic concepts of Physics behind PeTrack system is explained in detail. Sensitivity and distortion as two subjects to study in this project are introduced.

Chapter 2

Field of View and Simulation Studies

2.1 Overview

In this chapter the sensitivity and distortion of PeTrack system is studied using Monte Carlo simulation. The simulation is the most efficient method to study a system such as PeTrack which has a complicated geometry and an iterative algorithm. Moreover, all of the physics phenomena applied in PeTrack system are random therefore a Monte Carlo software is desirable for the simulation. The goals of simulation study are to examine the sensitivity and distortion of PeTrack, to study the possible effects of gaps between detector blocks on the sensitivity, and to determine the most effective field of view. Several simulations have been designed including simulation of prototype PeTrack system in order to investigate the sensitivity and distortion of PeTrack system.

2.2 Field of View (FOV)

As shown in Figure 1.7, each detector module of PeTrack includes 4 discrete detector blocks. Each detector block contains a 12×12 crystal array and each crystal element has a cross-sectional area of $3.9 \times 3.9 \text{ mm}^2$ with addition of 0.1 mm of Teflon film between them as reflective layer. Therefore, a

detector block has a cross section of $48 \times 48 \text{ mm}^2$. Since each detector module includes 4 detector blocks, the maximum possible FOV of the detector module also depends on the gap between the detector blocks (Figure 2.1). For example, the gaps for PeTrack prototype detector modules are 38 mm and 35 mm in y and z directions, respectively. Therefore the total area of coverage for each detector module is about $(4.8+3.8+4.8) \times (4.8+3.5+4.8) = 13.4 \times 13.1 \text{ cm}^2$. The reason of inserting gap in the structure of PeTrack module is to increase the FOV of the system without expanding the crystal size and adding PMTs. The coverage of detector modules increases with the gaps. However, it is expected that the sensitivity will not be uniform within the FOV. More importantly, the gaps may cause some low sensitivity or even blind spots within the FOV.

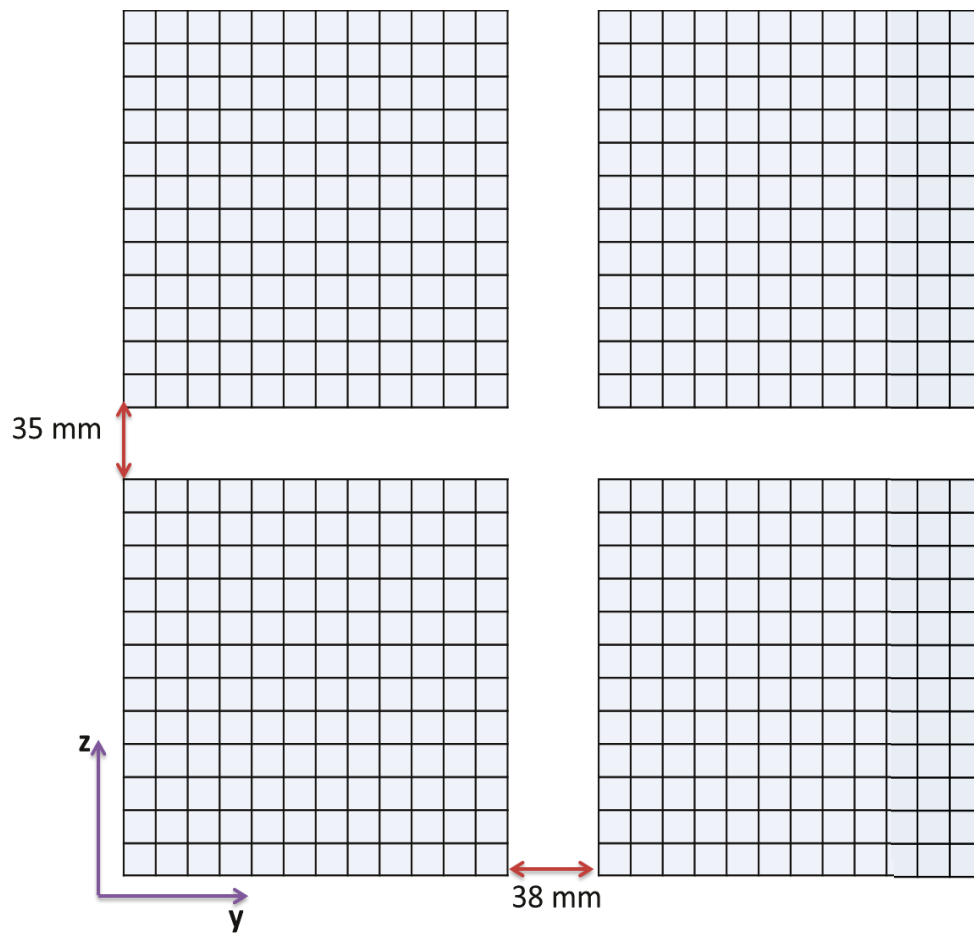


Figure 2.1: One detector module of prototype PeTrack with pixelate crystals and gap between the detector blocks.

Although it is desirable to have a large FOV, we have to select proper gaps to avoid blind spots. Since the geometry of PeTrack is complicated, it is difficult to calculate the sensitivity map within the FOV with geometric and algebraic methods. Simulation is the most efficient way to study the sensitivity of PeTrack. One of the goals of this project was to study different configurations of the detector blocks to find the optimal gap that can achieve an optimum FOV while maintain maximum sensitivity across the FOV. In order to do that, hundreds of points within the 3D volume of FOV have to be simulated and evaluated for their sensitivity for each configuration; which can be very time-consuming. Therefore, some tricks were used to reduce the simulation time. First, the simulation was not performed on individual detector-gap FOV configurations. Instead, I defined an ideal detector module which is a single block detector. The single block detector is a 38×38 array of BGO crystals which covers a bigger FOV ($152 \times 152 \text{ mm}^2$) compared to our prototype system ($134 \times 131 \text{ mm}^2$). The Monte Carlo simulation was done for a PeTrack system using two pairs of such big ideal detector modules and all the events were recorded. Then, the events were selected according to different gap-FOV configuration. The coloured regions represent the actual 12×12 array crystal blocks for each configuration. For example, the configuration A (pink in figure 2.2), has a gap of 4 crystals (16 mm) and FOV of $112 \times 112 \text{ mm}^2$. To mimic the simulation for configuration A, only the events that hit the pink crystals will be selected for source localization. This method allows us to reuse the same set of Monte Carlo data for many different gap-FOV configurations. Figure 2.2 shows the single module crystal with 3 different FOVs. In the figure the total single module detector is coloured in gray and all the other colours stand for different detector-gap FOV configurations.

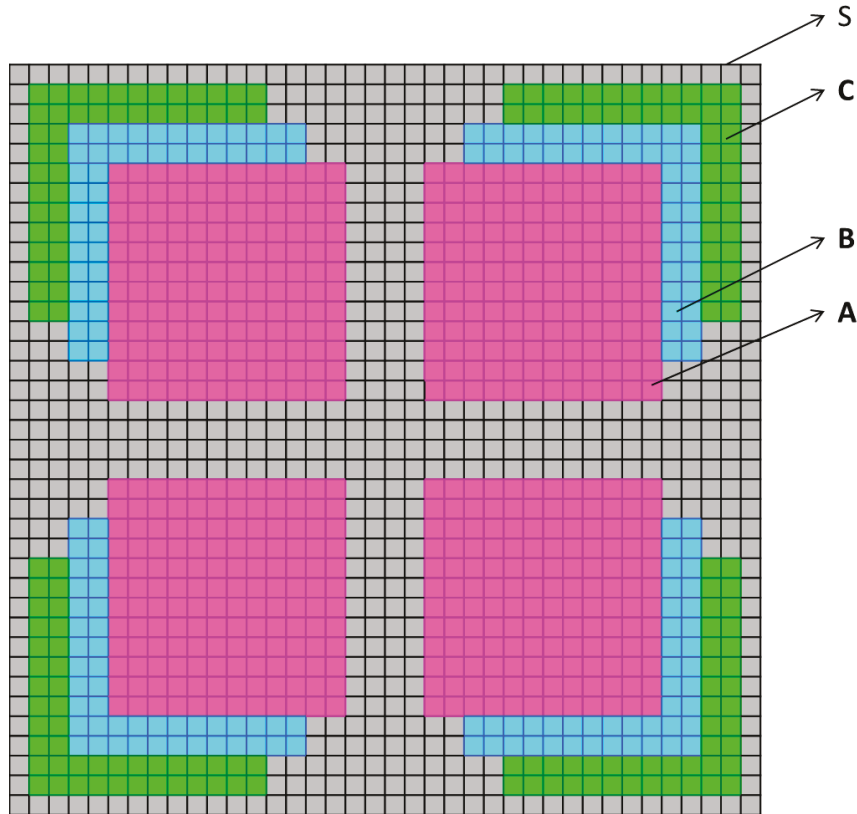


Figure 2.2: Single module detector and different detector configurations. The coloured regions represent the 12×12 array of crystal blocks.

2.3 Monte Carlo Simulation in GATE

There are various Monte Carlo codes able to simulate the traveling of the radiation through matter. I have chosen GATE for its robust detector modeling and time dependency that helps us to simulate a moving source [18].

2.3.1 Structure of GATE

The Geant4 Application for Tomographic Emission (GATE) is advanced software for Monte Carlo simulations in medical imaging. GATE is an open-source simulation toolkit which is developed by

the international Open-Gate collaboration. Currently, GATE is used for simulation of Positron Emission Tomography (PET) and Single Photon Emission Computed Tomography (SPECT), Computed Tomography (CT), and radiotherapy experiments. GATE is a user-friendly software since it is based on macro mechanism, i.e. the user can configure a simulation using macro scripts without writing computer code. Yet, it is still capable to simulate very sophisticated experiments [18].

2.3.2 Features of GATE

The most important feature of GATE is the time dependency. GATE models the passing of time during an experiment and the user is able to define the experiment timing. It results in the possibility of simulating the motion tracking in GATE. It provides the ability of modelling time-dependent phenomena, such as geometry element movements and source decay kinetics, allowing the simulation of time curves under realistic acquisition conditions [18].

2.4 Assembling the Simulation Elements

All components of the PeTrack system are defined in GATE using macro files. Different macro files define various parts of the PeTrack system such as detector geometry, source, capsules and etc. The main macro then makes reference to the each of these component macro files. Indeed to run a simulation the main macro needs to be executed. In order to survey the sensitivity and distortion throughout 3D FOV volume, a C++ code is written to define a 3D raster motion of a 0.5 mCi positron emitting point source (Figure 2.3). Because of the symmetric geometry, only 1/8 of the FOV volume was scanned by the raster motion, i.e. $0 \leq x \leq 7\text{cm}$, $0 \leq y \leq 7\text{cm}$, $0 \leq z \leq 7\text{cm}$. The sensitivity and distortion distribution in other regions is expected to mirror those of the simulated region. The step size for source motion is 0.5 cm within the y-z plane. Each y-z plane has a

different x location which starts at isocentre ($x = 0$ cm) of the PeTrack and ends at $x = 7$ cm with an incremental step of 0.5 cm. Therefore, there are $15 \times 15 = 225$ locations for each plane and the source stops for one second in each position which results in thousands of events for precise localization. The simulation is done on the EGS02 computer cluster in Physics Department, Carleton University. When 225 CPU cores are used, it took about 5 hours to simulate the raster motion within one y - z plane.

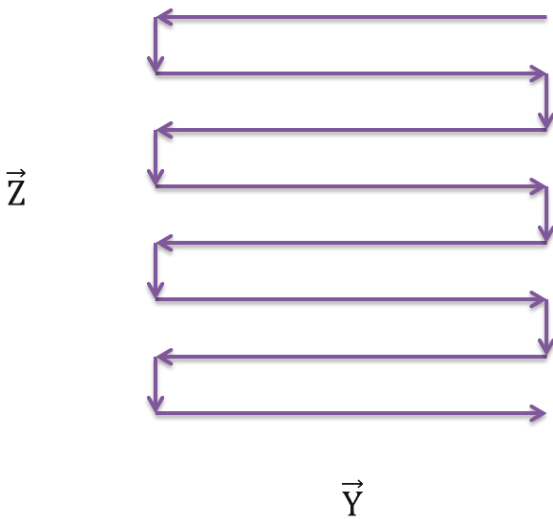


Figure 2.3: The raster motion defined for the source.

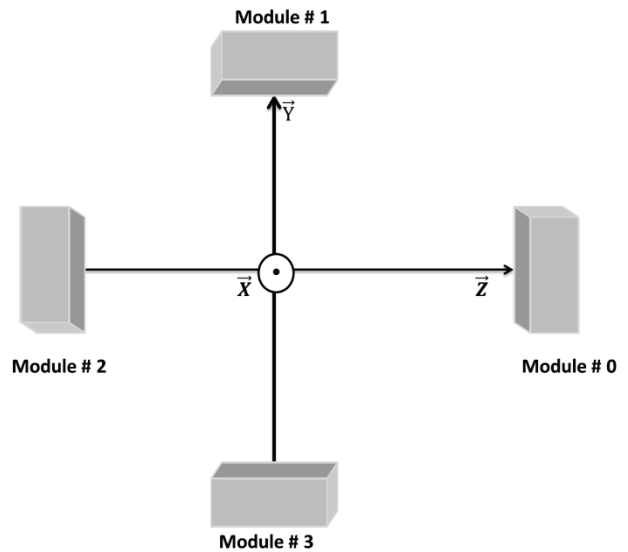


Figure 2.4: The alignments of PeTrack modules with respect to each other.

2.4.1 Detector

The geometry of the simulated PeTrack system is shown in Figure 2.4, which looks different from the photo shown in Figure 1.9 since PeTrack has to be rotated by 45 degrees in the laboratory frame to be integrated with x-ray C-arm. The smallest element of detector is one crystal element; in GATE each crystal element has a specific ID number. Each BGO crystal element has cross-section area of 3.9×3.9 mm² and 20 mm thickness. There is 0.1 mm of Teflon film between crystals to prevent scintillation light passing into the nearby crystals.

As describe in section 2.1, there is a 38×38 crystal element array inside one detector module. That module has the shape of a square $152 \times 152 \text{ mm}^2$ with 20 mm thickness. The detector module are placed at the distance of 475mm from the isocentre. The Figure 2.5 shows a 3D view of the four detector modules (Pink blocks) in GATE.

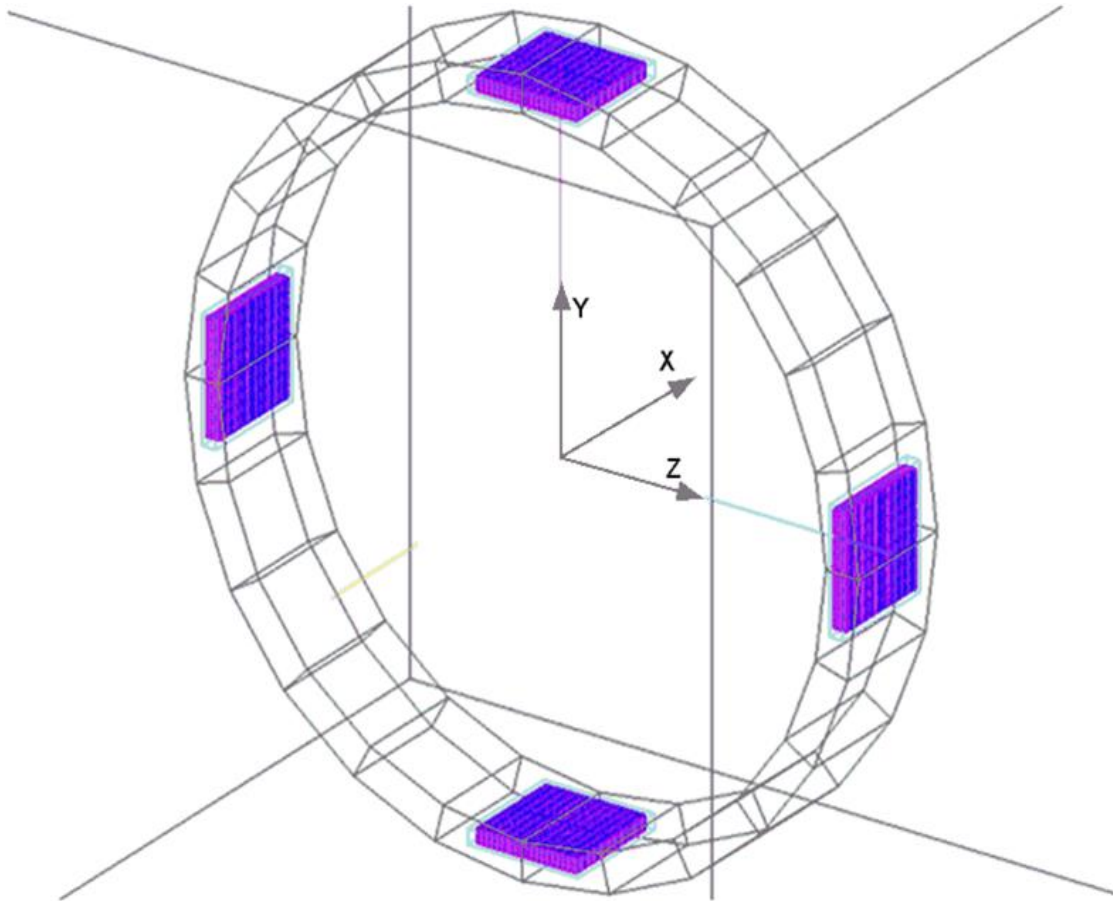


Figure 2.5: Simulated PeTrack system in GATE.

2.4.2 Physics

All of the possible interactions of radiation with matter are defined in Physics macro. For example, photoelectric, Compton, Rayleigh scattering, electron ionization, bremsstrahlung, positron annihilation, and radioactive decay.

2.4.3 Digitizer

The electronics of the PeTrack detector are defined in the digitizer macro file. There are two pulse grouping components. The energy of reference is set to 511 keV. The Energy window is between 420 keV and 600 keV, therefore the detectors are configured for annihilation gamma rays.

2.4.4 Source

The shape of introduced point source for simulation is sphere with a radius of 0.25 mm. The source is Sodium-22 with half-life of 2.6 years which decays to Neon-22. The activity of the source is 0.5 mCi. The source is positioned at the centre of a gold capsule.

2.4.5 Capsule

In simulation the source is inserted inside a capsule in order to restrict the range of positron. The capsule has a shape of sphere with interior radius of 0.25 mm and external radius of 0.45 mm and its material is set to be Gold. In the simulation a raster motion is defined for the source, since source has been attached to a capsule therefore the capsule will follow the same motion pattern.

2.5 Selection of Different Detector Configurations

As described in section 2.1, the simulation has been done for the single ideal module detector (S) configuration in Figure 2.2 and all the events are recorded in the format of ROOT file [19]. Then, data can be selected in a way which represents in either configurations A, B, or C as shown in Figure 2.2.

2.5.1 Simulation Data Processing

The simulation has been done individually for each y-z plane with a constant x. A ROOT script file was written to process the event data, which is stored in ROOT format files. The script first selects only the events that hit the crystal elements within the detector block specified by the gap-FOV configuration, for example, the pink crystals illustrates configuration A in Figure 2.2. The selection was done by checking the crystal IDs stored with the events. The next step is to calculate the (x, y, z) coordinates of the location that is hit by the photon on the detector crystals. These locations are calculated from the isocentre of the PeTrack system. Each coincident event includes two locations hit by the two gamma rays. A line connecting these two locations forms the coincident line, or line of responses, LOR. Therefore, the ROOT script makes it possible to select a desired FOV based on crystal IDs and obtain the corresponding LORs. Once the LOR data are extracted the next step is to track the position of the source in 3D using a LabView implementation of PeTrack algorithm [20]. The final step in data processing is the comparison of the tracked source position with the true source locations. This is accomplished using a code in MATLAB which calculated the error of simulation results and displays the sensitivity and error maps for the results [21].

2.6 Results of Different Detector Configurations

A quarter of the FOV for each x plane is depicted for all of the sensitivity and error maps. The acceptable accuracy for real-time tracking is 2 mm in medicine [1, 24]. Therefore, all of the color bars in the error maps have a range of ± 2 mm. The threshold for the effective FOVs is determined based on the error maps i.e. while the error map shows an error less than 2 mm for a plane, that plane will be considered inside the FOV. Moreover, within each plane the effective FOV is the

region with error less than 2 mm. The sensitivity is considered for the regions which are inside the FOV.

2.6.1 Sensitivity and Error Maps of Configuration A

This configuration as shown in Figure 2.2 (pink blocks) has 4 crystal-sized gaps between detector blocks. It has the theoretical FOV area of $(12 \times 0.4 + 4 \times 0.4 + 12 \times 0.4) + (12 \times 0.4 + 4 \times 0.4 + 12 \times 0.4) = 11.2 \times 11.2 \text{ cm}^2$. Figure 2.6 shows the sensitivity map of detector A.

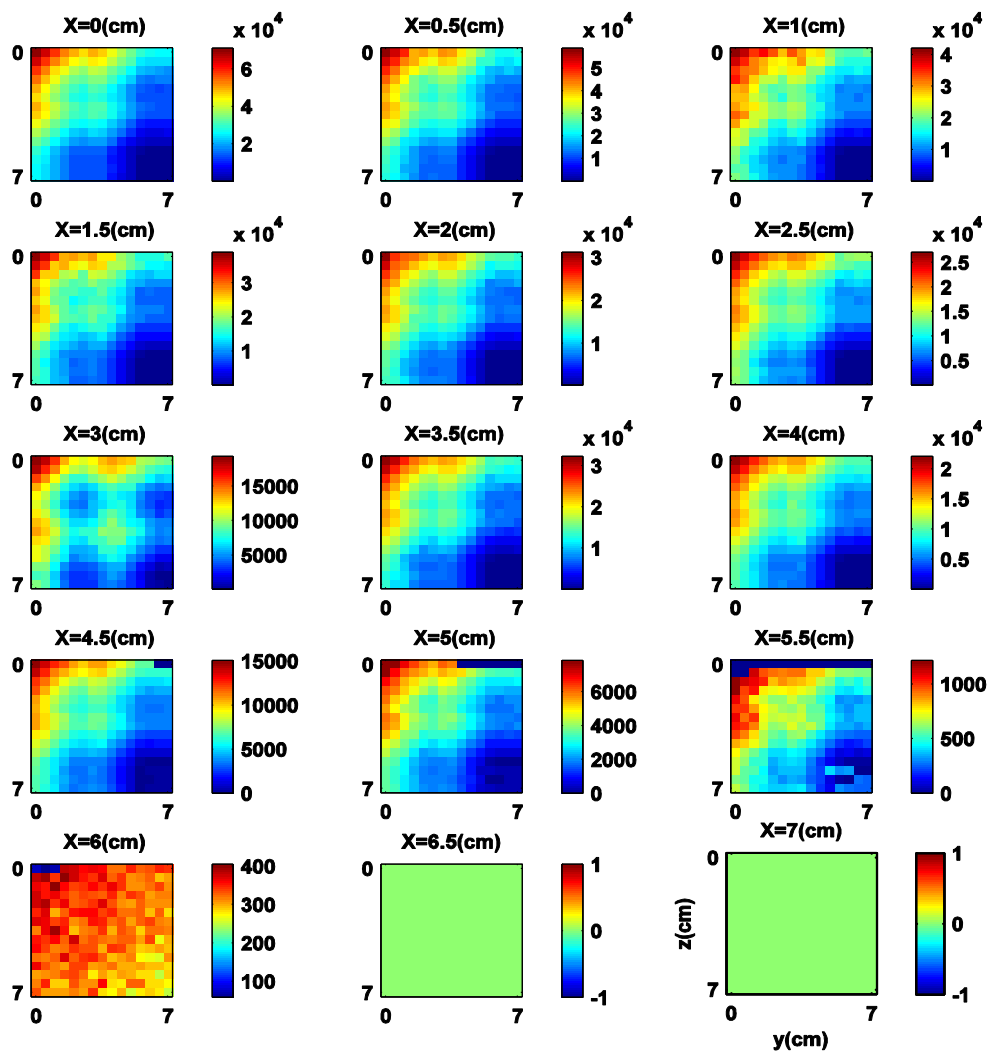


Figure 2.6: The sensitivity map of configuration A. The horizontal and vertical axes in each graph are y-axis (in cm) and z-axis (in cm), respectively. The sensitivity is represented by count/sec/ (0.5mCi).

According to the geometry of PeTrack the plane which is located at the centre of the FOV has the highest number of counts. At the distance 3.5 cm away from the isocentre the sensitivity drops to about 50% of that of the centre. The minimum observed sensitivity belongs to the plane which is located at the distance of $x=6$ cm from the isocentre.

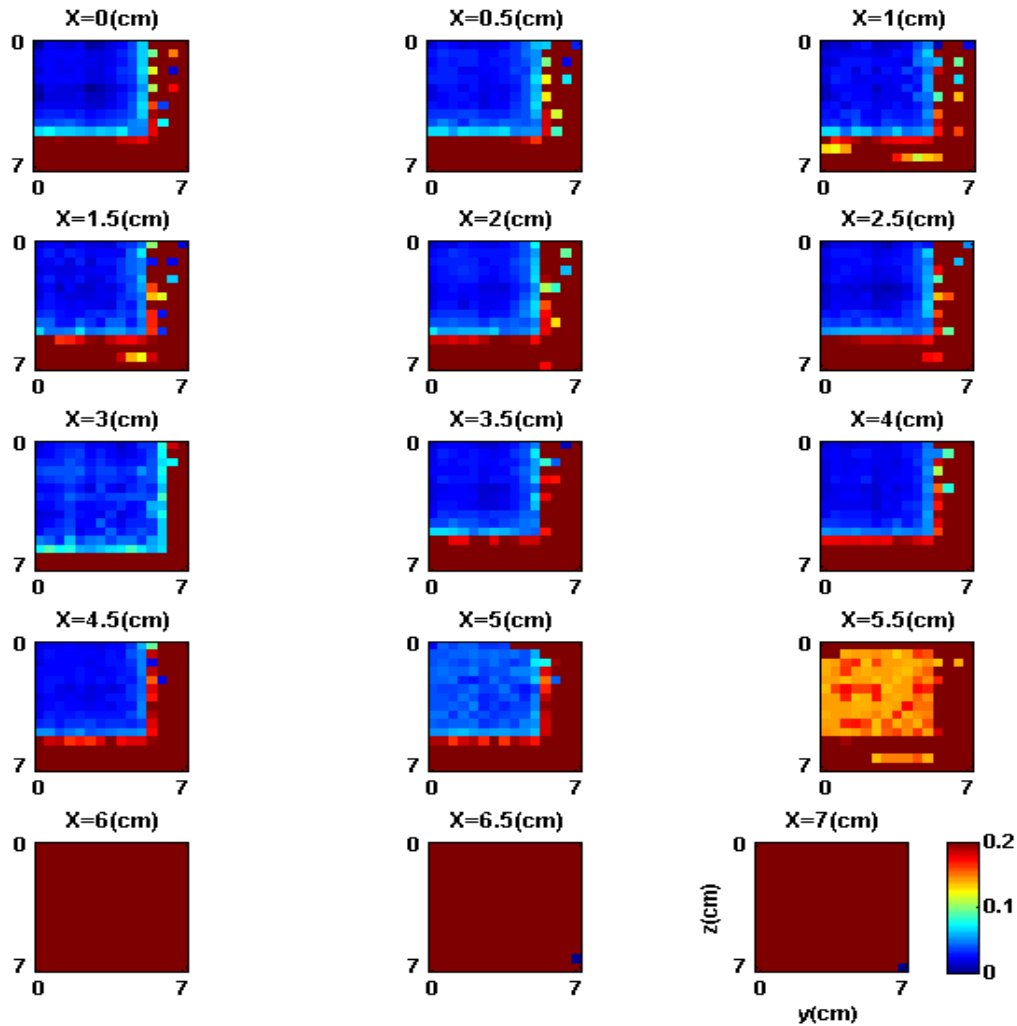


Figure 2.7: The sensitivity map of configuration A. The horizontal and vertical axes in each graph are y-axis (in cm) and z-axis (in cm). All units are in cm including the color bar. The error map also indicates the boundary of the effective FOV which is ± 5.5 cm in all direction for this configuration.

Figure 2.7 shows the total error map for configuration A. The total error is calculated based on equation 2.1:

$$\text{Total Error} = \sqrt{(x_2 - x_1)^2 + (y_2 - y_1)^2 + (z_2 - z_1)^2} \quad (2.1)$$

Where (x_1, y_1, z_1) is the true location of the source and (x_2, y_2, z_2) is the tracked location by simulated PeTrack system. Regarding to the error map the threshold of FOV for configuration A is set to be at $x = 5.5$ cm. The error map also indicates that within the FOV the error is less than 1 mm. The planes located at $x = 6$ cm $x = 6.5$ cm and $x = 7$ cm show an error of 2 mm and are considered to be outside of the FOV.

2.6.2 Sensitivity and Error Map of Configuration B

Configuration B as shown in Figure 2.2 (blue blocks) has 8 crystal-sized gap with the theoretical FOV area of 12.8×12.8 cm². Figure 2.8 shows the sensitivity maps for configuration B.

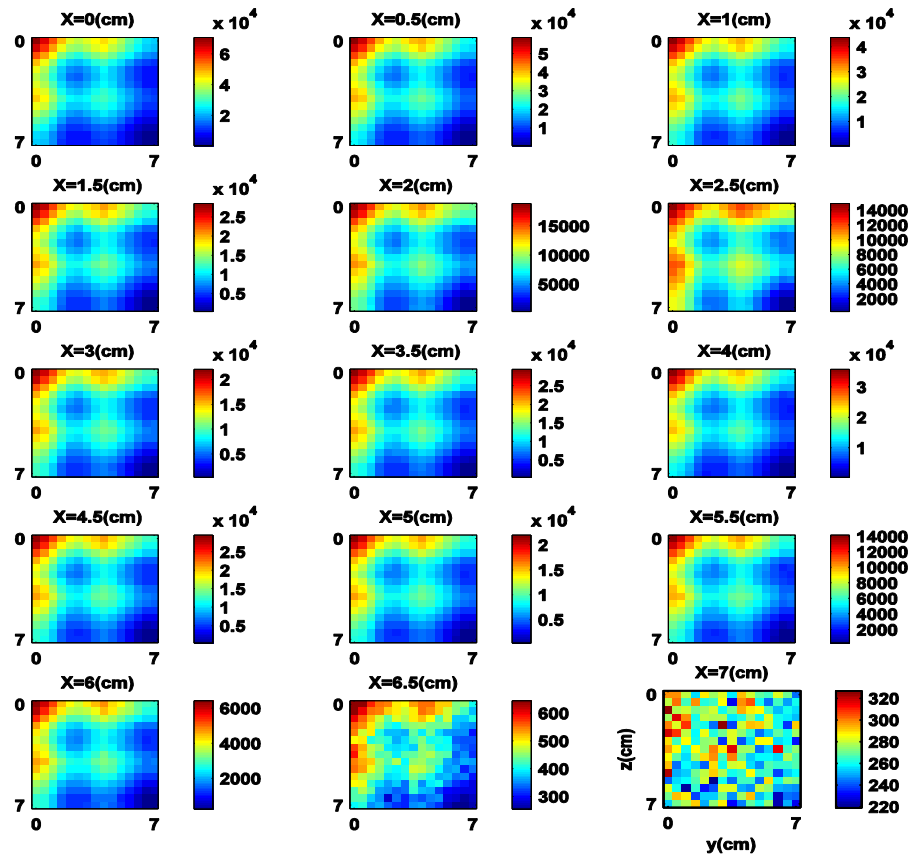


Figure 2.8: The sensitivity map of configuration B. The horizontal and vertical axes in each graph are y-axis (in cm) and z-axis (in cm). The sensitivity is represented by count/sec/ (0.5mCi). By increasing the gap a structure in sensitivity map is observed.

By increasing the gap between detector blocks, some low sensitivity regions (cold spot) are now visible at $(y = 2.5, z = 2.5)$ in each x-plane. The sensitivity is maximum at the isocentre (6×10^4) which drops to 6×10^3 at $x = 6$ cm.

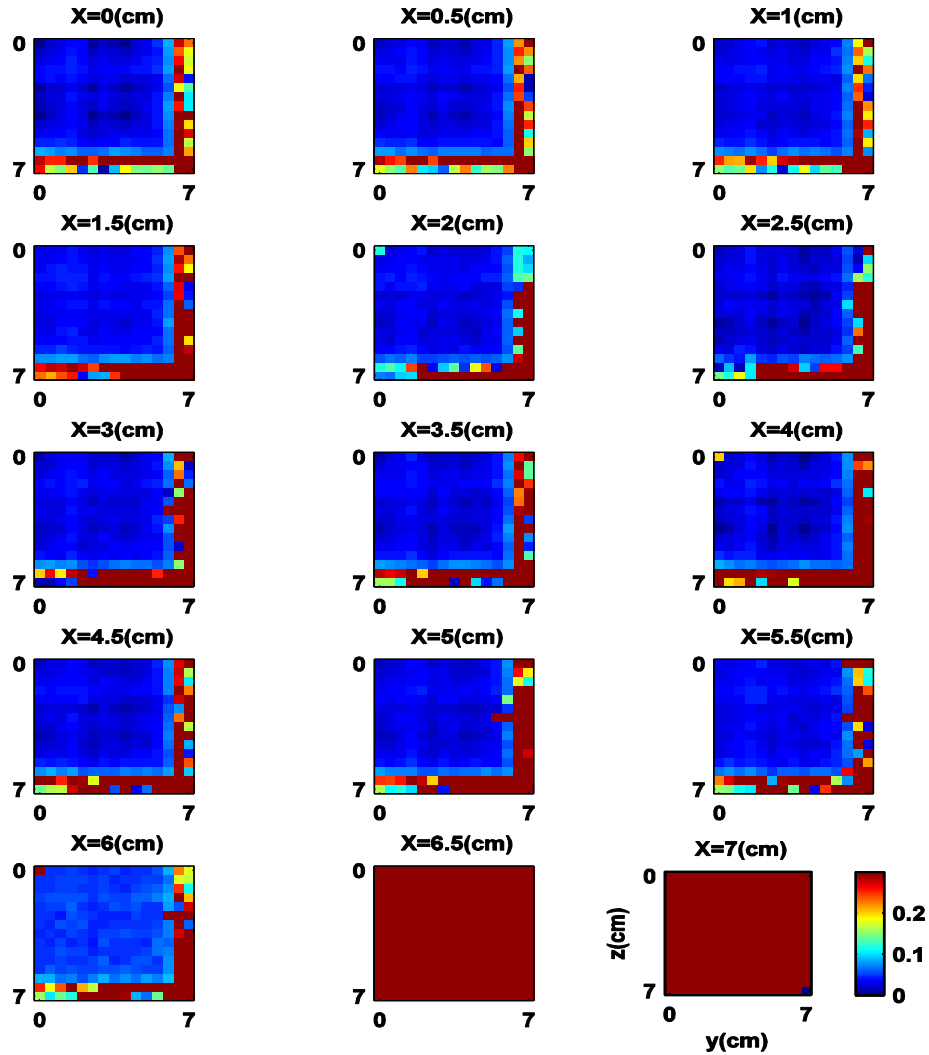


Figure 2.9: The sensitivity map of configuration B. The horizontal and vertical axes in each graph are y-axis (in cm) and z-axis (in cm). All units are in cm including the color bar. The error map also indicates the boundary of the effective FOV which is at ± 6 cm in all directions for this configuration.

Configuration B is similar to the prototype PeTrack detector. Comparing to error map of A, configuration B has larger area of effective FOV which is about ± 6 cm in all directions. The high error (> 2 mm) region is coincident with the low sensitivity regions in Figure 2.8.

2.6.3 Sensitivity and Error Map of Configuration C

The configuration C as shown in Figure 2.2 (green blocks) has 12 crystal-sized gap between detector blocks. It has the theoretical FOV area of $14.4 \times 14.4 \text{ cm}^2$.

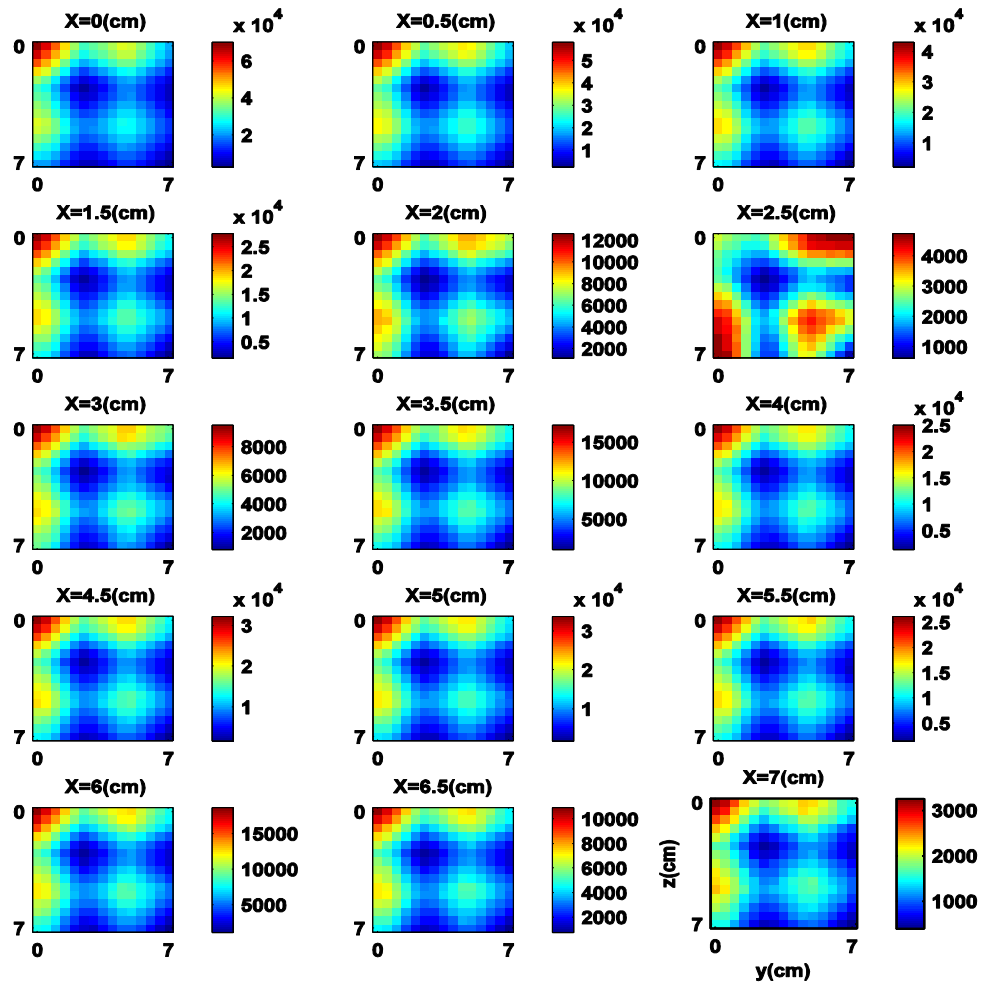


Figure 2.10: The sensitivity map of configuration C. The horizontal and vertical axes in each graph are y-axis and z-axis, respectively. The sensitivity is represented by count/sec/ (0.5mCi). The structure is clearer. A bigger gap results in the cold spots.

Comparing to detector A and B detector C has the largest FOV. The structure on the sensitivity map is become clearer. The cold spot at $(y = 2.5, z = 2.5)$ become even darker, indicating lower sensitivity at these regions which is 616 count/sec/mCi. In Configuration C, sensitivity is the

maximum at the edge of FOV which results the minimum counts drop between isocentre and the edge of FOV.

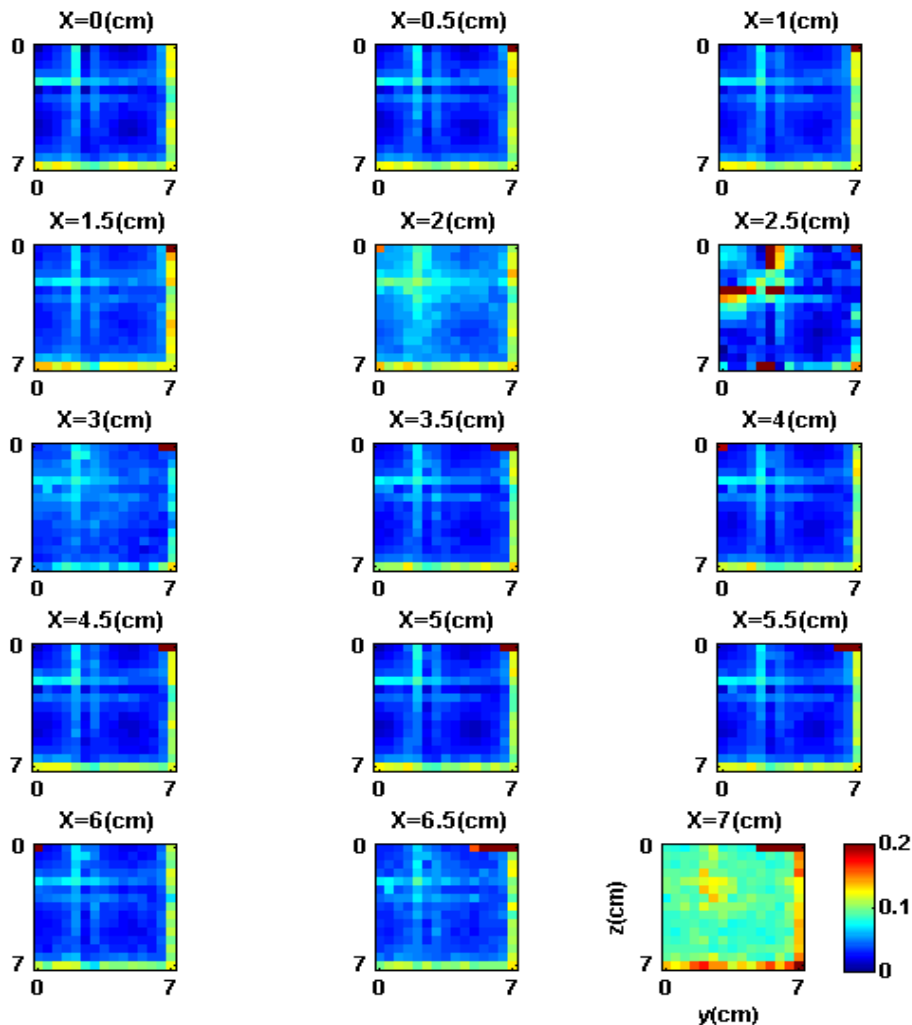


Figure 2.11: The total error map of configuration C. The horizontal and vertical axes in each graph are y-axis (in cm) and z-axis (in cm). All units are in cm including the color bar. The error map also indicates the boundary of the effective FOV which is at ± 7 cm in the all directions for this configuration.

Figure 2.11 shows the total error maps of configuration C. It clearly has the largest effective FOV coverage and the threshold for the effective FOV can be set at $x=6.5$ cm. However, large errors can be seen at $x=2.5$ cm plane, which is corresponding to the cold spot on the sensitivity map.

2.7 Simulation of PeTrack Prototype

A simulation was also designed in GATE to study the actual prototype PeTrack system. The detector macro was altered from single block module to the actual 4-block PeTrack detector. The size of the crystal elements and its material remained the same. Each of the four detector blocks in one module contains a 12×12 crystal array. The gaps between the blocks are 38 mm in y or z direction, and 35 mm in x direction. The activity of the source altered to 1 mCi. The method of the simulation is similar to the single module detector. The raster motion is defined on the y-z planes with step size of 1 cm. Unlike the raster motion used in section 2.3, the raster scan of the source covers the entire FOV within each y-z plane. These y-z planes were placed 1 cm starting from the isocentre to $x=6$ cm in both negative and positive x direction. Due to the symmetric geometry of the prototype system, the simulation was only performed for positive x planes. The following figures show the results of the sensitivity and error studies for prototype PeTrack. The results of the simulation for the prototype system were studied for the two main characteristics of PeTrack: sensitivity and distortion. The sensitivity map covers the overall FOV.

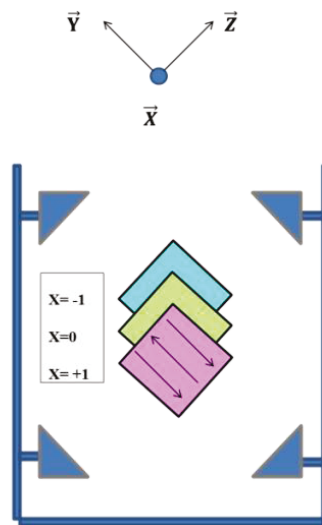


Figure 2.12: The Prototype PeTrack geometry showing the raster motion of the source on the planes.

2.7.1 Results of the Prototype PeTrack

Figure 2.13 shows the sensitivity map of prototype PeTrack. The structure of FOV is completely shown in this figure since the simulation has been done for overall FOV.

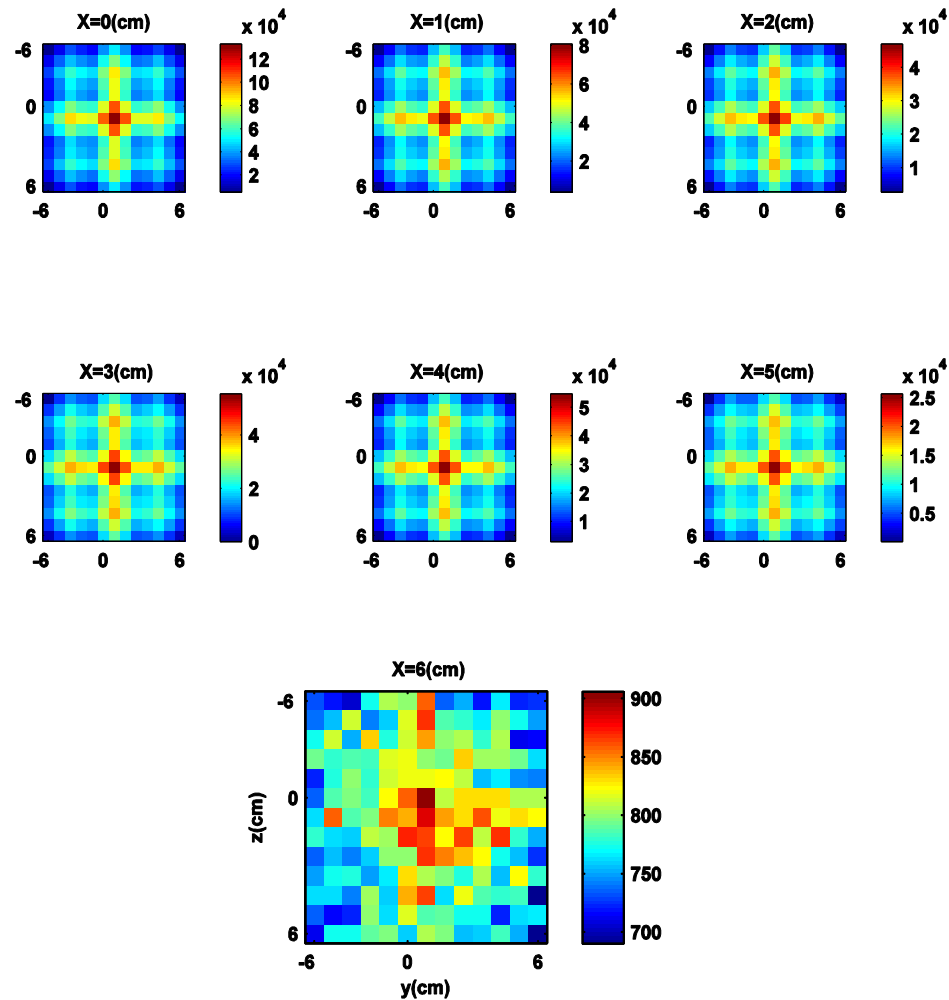


Figure 2.13: The sensitivity map of prototype PeTrack. The horizontal and vertical axes in each graph are y-axis and z-axis, respectively. The sensitivity is represented by count/sec/ (1mCi).

The total error is calculated by equation (2.1) and it illustrates an error about 1 mm at the edge of the FOV (Figure 2.14). Plane $x=6$ cm has the maximum error since it is outside of the FOV. The range of color bar is set from -0.2 to 0.2 in order to show the expansion and shrinking in the error map of prototype PeTrack.

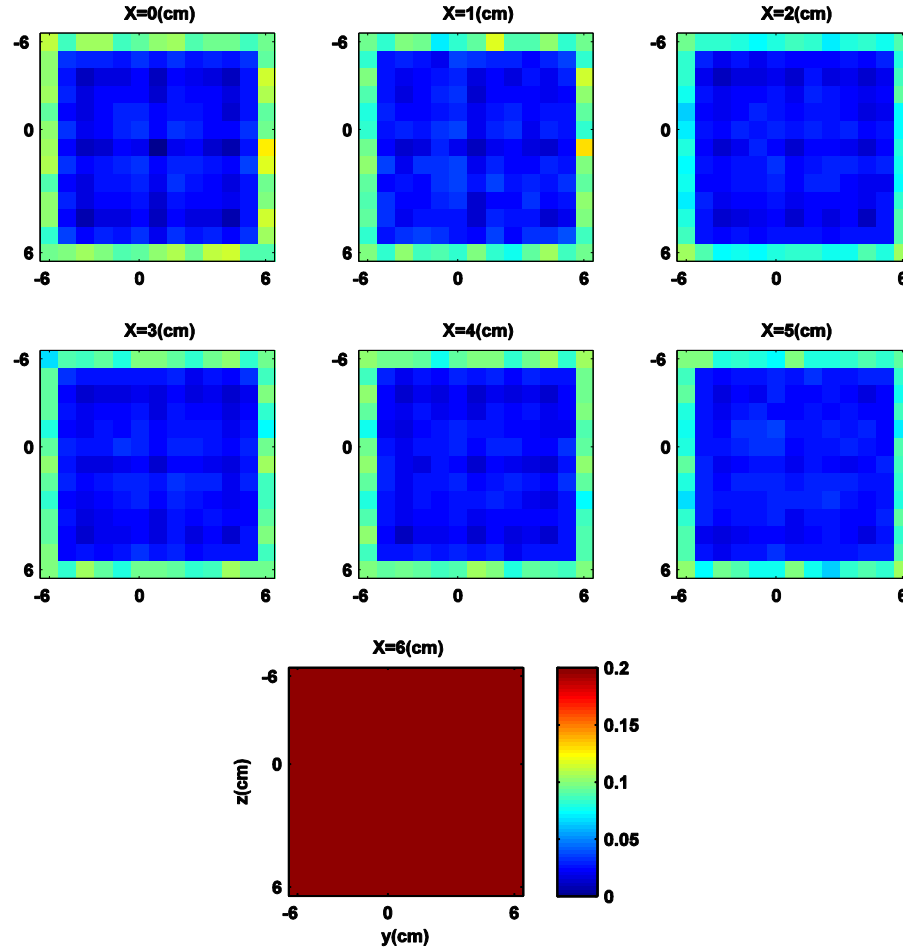


Figure 2.14: The total error map of prototype PeTrack. The horizontal and vertical axes in each graph are y-axis (in cm) and z-axis (in cm). All units are in cm including the color bar. The error map also indicates the boundary of the effective FOV which is at ± 5 cm. The error map indicates that the absolute error within the effective FOV is less than 1 mm within the FOV.

While Figure 2.14 shows the total 3D error map, it is important to investigate the (x, y, z) components of the error in order to have a better idea of any systematic distortions. The component error in x direction is calculated by equation 2.2:

$$\text{Component Error} = \text{sign}(x_{\text{true}}) (x_{\text{tracked}} - x_{\text{true}}) \quad (2.2)$$

Where x_{true} is the true coordinate of the source and x_{tracked} is the coordinate reported by PeTrack.

The component error can be calculated for y and z directions as above. Figure 2.15 shows the component error in z direction.

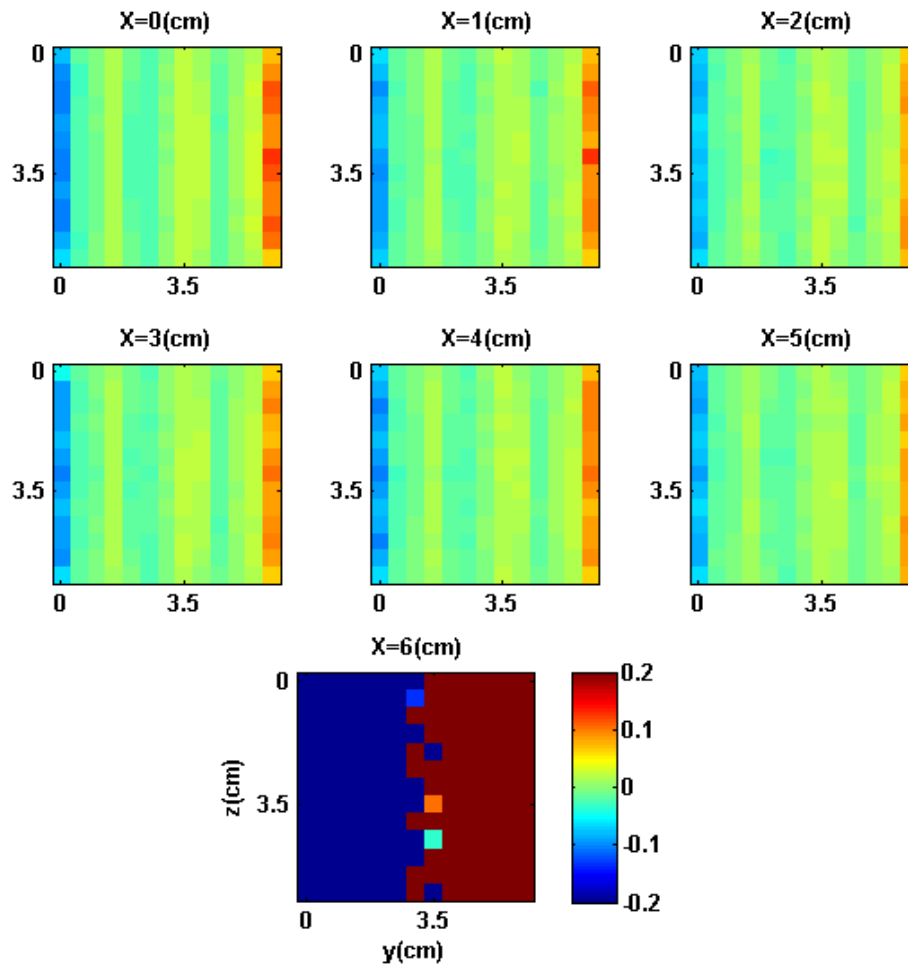


Figure 2.15: The error map of prototype detector in z direction. The horizontal and vertical axes in each graph are y -axis (in cm) and z -axis (in cm). All units are in cm including the color bar. The tracked locations in the yellow and blue regions along z axis are expanded and shrunk, respectively.

Figure 2.15 shows strips of positive (yellow) and negative (blue) values. This indicates overestimate (in yellow regions) and underestimate (in blue regions) of tracked z -coordinate as compared with the true source coordinate. The clearly striped pattern indicates a systematic distortion of expansion or shrinking inside the effective FOV. However the amplitude of the distortion is smaller than 0.1 mm.

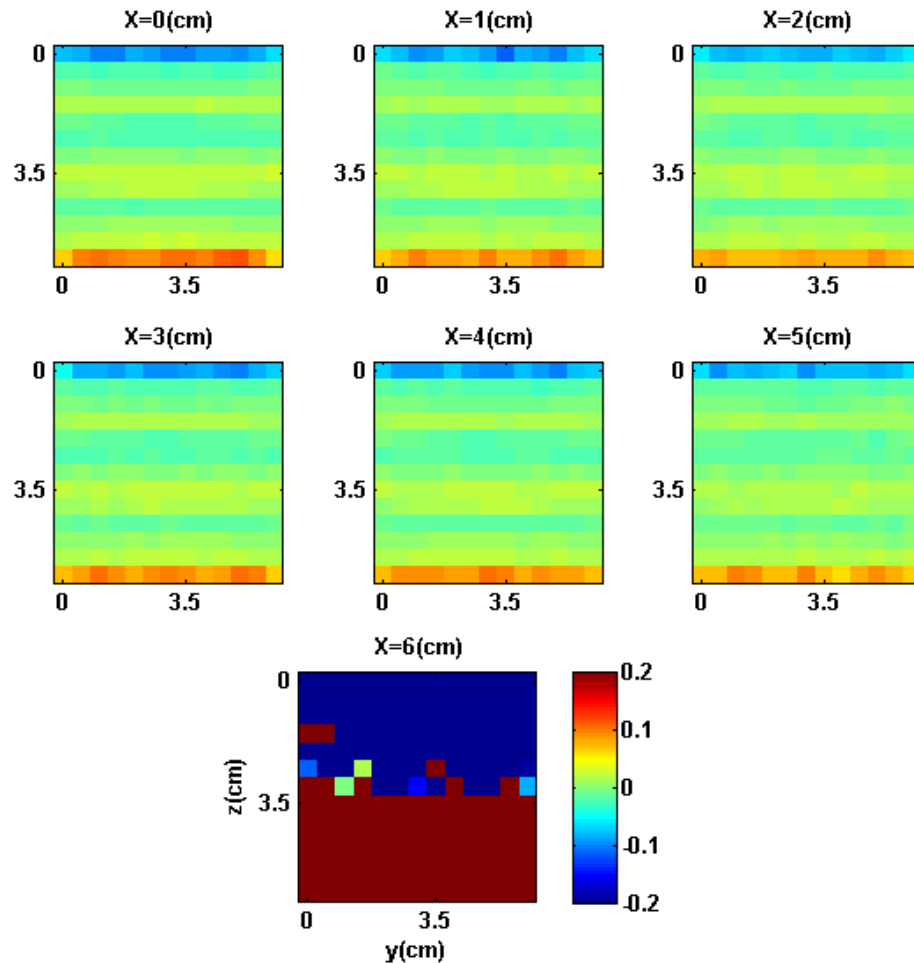


Figure 2.16: The error map of prototype detector in y direction. The horizontal and vertical axes in each graph are y -axis (in cm) and z -axis (in cm). All units are in cm including the color bar. The tracked locations in the yellow and blue regions along y axis are expanded and shrunk, respectively. The tracked locations in the yellow and blue regions are expanded and shrunk, respectively.

The error maps in Figure 2.16 illustrate similar expansion and shrinking along y axis as well which is repeated across the effective FOV.

Figure 2.17 shows the error maps of x component. The error along x direction is uniform within the y - z plane; however, the systematic distortion changes from plane to plane, as indicated by their different colors. Most of the distortion in the x direction is shrinking (indicated by bluish green color) except at plane $x=3$ cm.

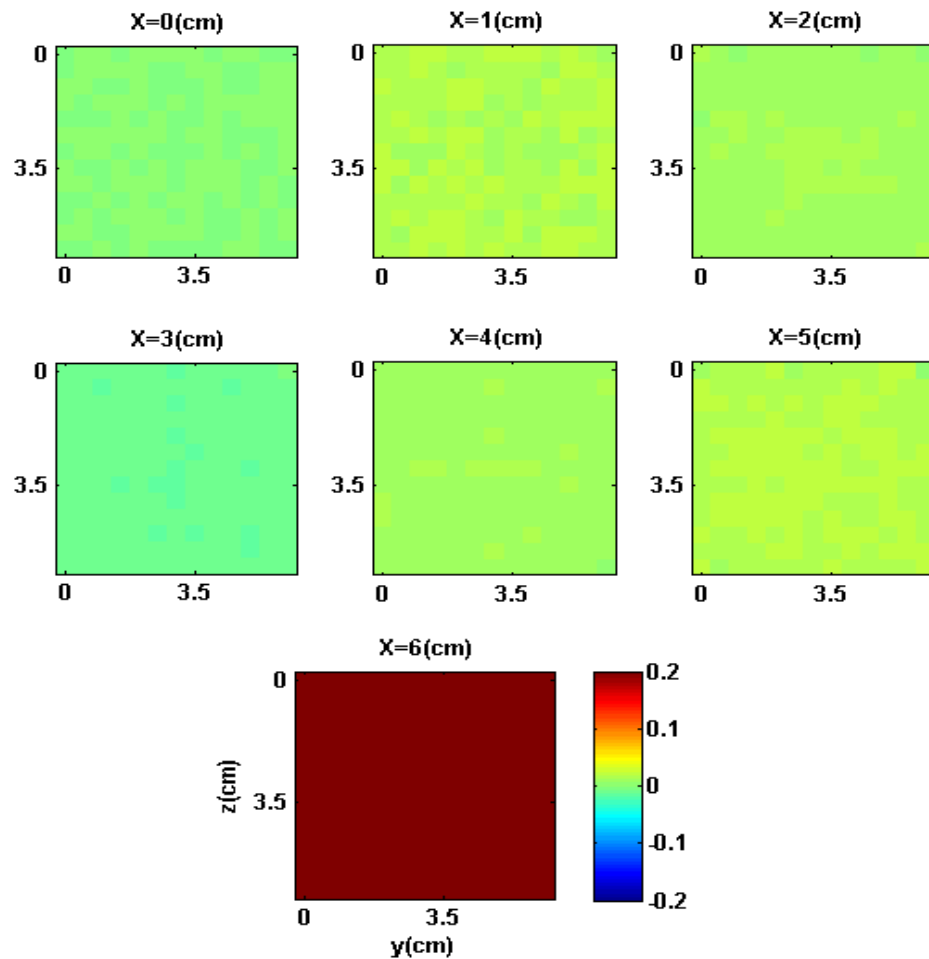


Figure 2.17: The error map of prototype detector in x direction. The horizontal and vertical axes in each graph are y-axis (in cm) and z-axis (in cm). All units are in cm including the color bar. The tracked locations in the yellow and blue regions are expanded and shrunk, respectively. The error map shows a non-uniform distortion.

Figure 2.17 shows the error maps of x component. The error along x direction is uniform within the y-z plane; however, the systematic distortion changes from plane to plane, as indicated by their different colors. Most of the distortion in the x direction is shrinking (indicated by bluish green color) except at plane $x=3$ cm.

2.8 Graphical Interpretation of the Results

Figures 2.18 (a) and 2.18 (b) compare the FOV of two different cases: without detector block gap and with the gap. When there is no gap between detector blocks the FOV is limited to the cross section of the detector blocks as shown in Figure 2.18a. However, applying gaps increases the potential volume that annihilation can be detected. Depending on the location of the annihilation, there will be different structures for sensitivity graphs as shown in the results section. In Figure 2.18 (b), the annihilations that occurred in the region 1 is limited to be seen by detector blocks A1 and B1, the situation is the same for region 2. By inserting a gap between 2 detector blocks there are more regions that detector blocks can detect the annihilation such as regions 3, 4, and 5 in figure 2.18 (b).

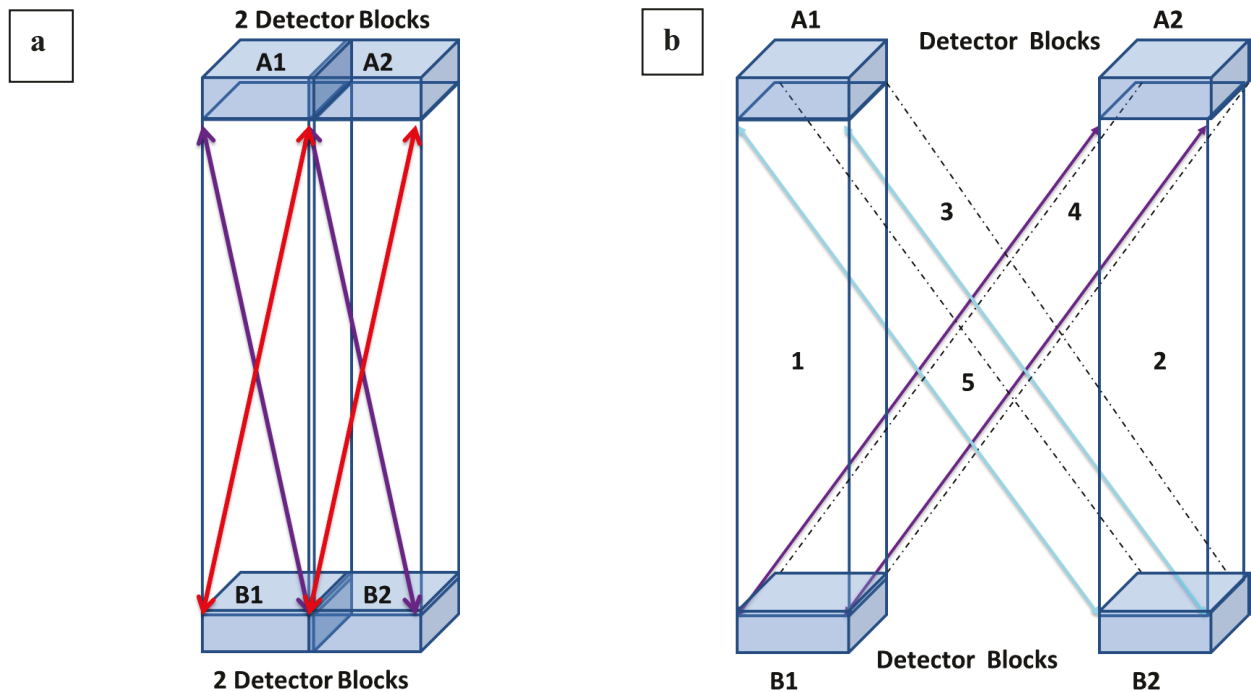


Figure 2.18: (a) Two detector blocks without gap between them. (b) Two detector blocks with gap between them.

Meanwhile, inserting the gap creates the blind areas where the annihilations inside them are not detectable with any opposite pairs of detectors. The blind regions are located between 2 detectable regions, such as the triangular region between region 1, 2, and 5. Note that there are 4 pairs of

detector blocks in actual PeTrack system; however, only 2 pair of them is shown here for the simplicity of the figure.

2.9 Discussion

Using GATE simulation package different configuration of PeTrack system is defined and simulated. The results of simulation studies clearly indicate the boundary of the FOV for the different detector configurations. The results show that FOV can be enlarged by inserting the gap between the detector blocks. However, low sensitivity regions starts to appear in the middle of the FOV and eventually become a blind spot when the gap is large enough(detector configuration C). The errors for the entire detectors configuration are studied. The errors within the FOV are less than 1 mm except at the blind spot of configuration C or close to the edge of FOV. In the prototype simulation the sensitivity map shows a 92% drop in the number of counts when the source moved from the isocentre to the plane $x=6$ cm which is outside of the FOV. The total error map in figure 2.14 indicates that the prototype PeTrack has an effective FOV of about 11×11 cm² and the error is about 0.5 mm inside the FOV. The repeated pattern in the error map in x, z and y directions address indicate the systematic distortion in the PeTrack system which will be investigated more in the following chapters.

2.10 Summary

In this chapter the sensitivity and distortion were studied on the different configurations of PeTrack including the prototype PeTrack. The Monte Carlo simulation allowed us to simulate the different gap-detector configurations and study the effects of gaps on sensitivity, distortion, and determine an optimum FOV. The observed results for sensitivity and error maps revealed that the maximum

sensitivity and minimum error happens at the isocentre of each configuration. The boundary of FOV became clear for each configuration based on the error map. Inserting the gap between detector blocks increased the coverage of FOV. However it can degrade the sensitivity map as results of configuration C showed that the bigger gap creates the cold or even blind spots in the sensitivity map and introduce an unacceptable error inside the FOV. The results of simulation for prototype PeTrack declared the threshold of FOV and indicated that the PeTrack system is locally distorted.

Chapter 3

The Effects of Misalignment

3.1 Overview

In chapter 2, I studied different detector configurations. The goal of this chapter is to study the effect of geometric misalignments on PeTrack. The misalignment is introduced to detector B configuration in Figure 2.2 which contains 8 crystal-size gaps. The configuration B has chosen to introduce the misalignment since its size is similar to the prototype. Moreover, based on the results of chapter 2, configuration B is nominated as an optimum configuration for PeTrack system. The sensitivity and deviation maps of misaligned detectors are studied.

3.2 Misalignment

The subject of misalignment is introduced in this project in order to examine its effects on the PeTrack. Misalignment occurs when a pair of the detector modules is not exactly in the contrary position with respect to each other (Figure 3.1). Theoretically, misalignment should not affect the tracking accuracy as long as the misalignment is known and taken into account when calculating

the line of response (LOR) from crystal IDs. However, in practice, the actual misalignment may not be precisely known. It would be interesting to study the effects of misalignment on the accuracy of tracking. Regarding to the geometry of PeTrack different types of misalignments could be introduced. In this chapter, two types of misalignment will be studied.

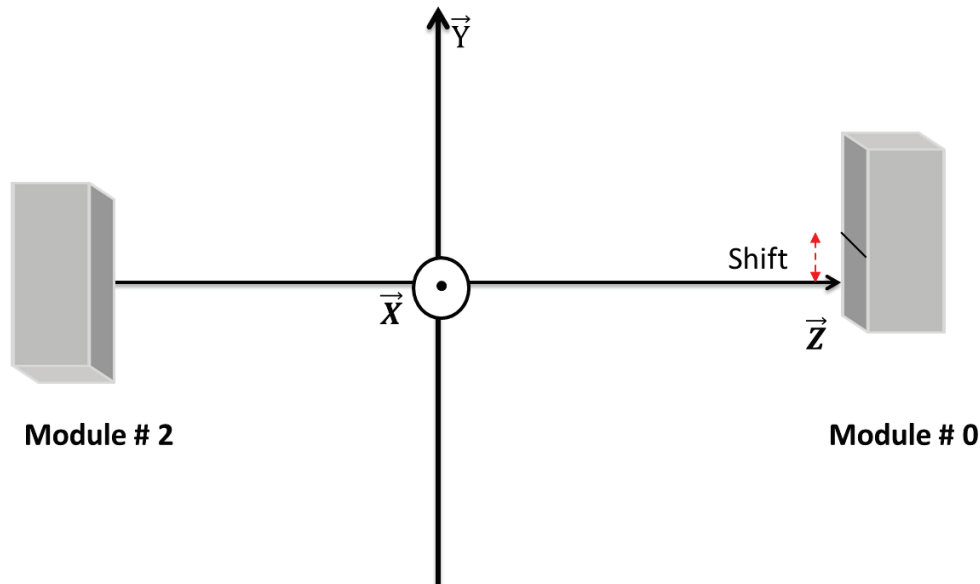


Figure 3.1: The misalignment is introduced to the system when detector blocks are shifted with respect to each other.

3.2.1 Introducing a Misalignment

The most efficient way of introducing the misalignment and studying its effects on the PeTrack system is simulation. The results of the simulation in chapter 2 cover the sensitivity and error maps for three different FOV configurations, namely A, B, and C. Among them the configuration B is chosen to study for the misalignments since it is similar to the prototype PeTrack in terms of gaps and FOV size. The misalignment is introduced by shifting the crystal blocks in Figure 2.2 by a couple rows or columns of crystal in only one of the modules. The misalignment is implemented in the event selection ROOT script (see section 2.4.1) [19]. The event is selected based on shifted crystal blocks; however, LOR was calculated assuming there is

no shift, which simulates the “unknown” misalignment (Figure 3.1). Two misalignment cases were simulated. In first case, the module # 0 is shifted by 8 mm in x direction; in the second case module #2 is shifted by 8 mm in y direction (Figure 3.2). Although both shifts are shown in this figure, they are implemented in two different simulations.

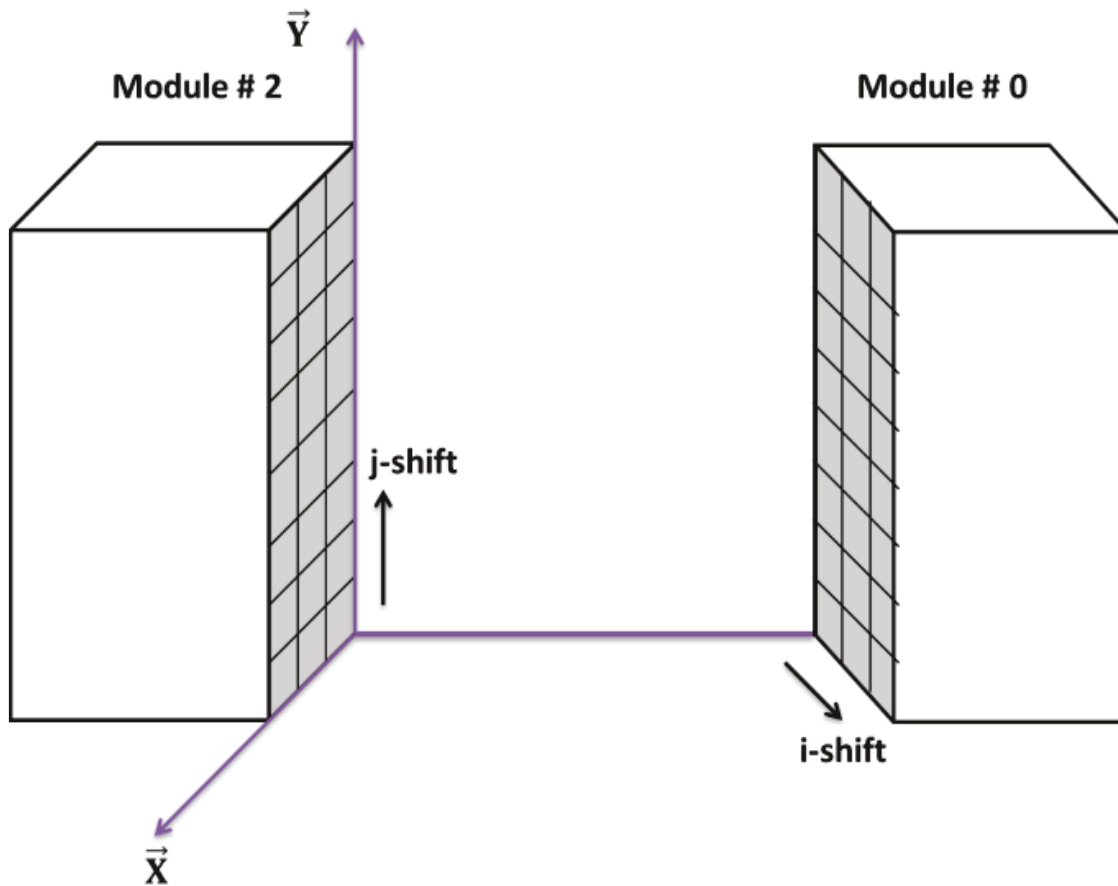


Figure 3.2: Shifting the crystals in x direction (i-shift) and y direction (j-shift). Although both shifts are shown in this figure, they are implemented in two different simulations.

3.3 Results of Misalignment in X Direction

In chapter 2 the error map are studied for the threshold of 2 mm. It is predicted that the misalignment may introduce larger error to the system, thus in this chapter the threshold for the error maps is increased to 5 mm.

Figure 3.3 illustrates the sensitivity map for shifting two crystals in x direction.

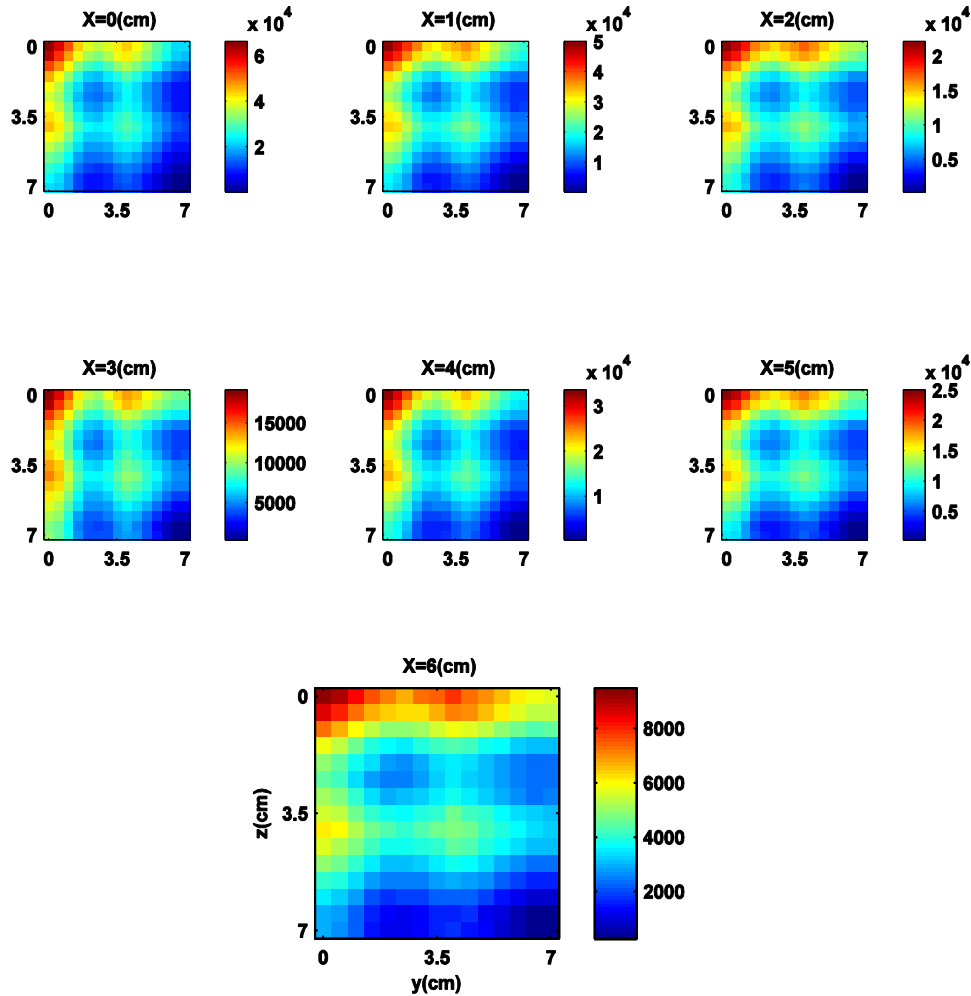


Figure 3.3: The sensitivity map of i-shift is shifted upward with respect to configuration B. The sensitivity is represented by count/sec/ (0.5mCi). The horizontal and vertical axes in each graph are y-axis (in cm) and z-axis (in cm), respectively. By shifting 8 mm in x direction the structure of sensitivity map has stretched.

Comparing Figure 2.8 with the figure above shows that shifting 8 mm in x direction does not affect the sensitivity in y-z plane. However, by shifting the crystals the structure of the sensitivity map seems to be “stretched” in the y direction at y-z plane with larger x values.

Figure 3.4 depicts the error map of i-shift. The error map of misalignment in x direction shows an error of up to 5 mm. In i-shift the crystals are shifted in x direction; therefore, most of the error is observed in this direction contribute to the misaligned pairs: Module #0 and #2.

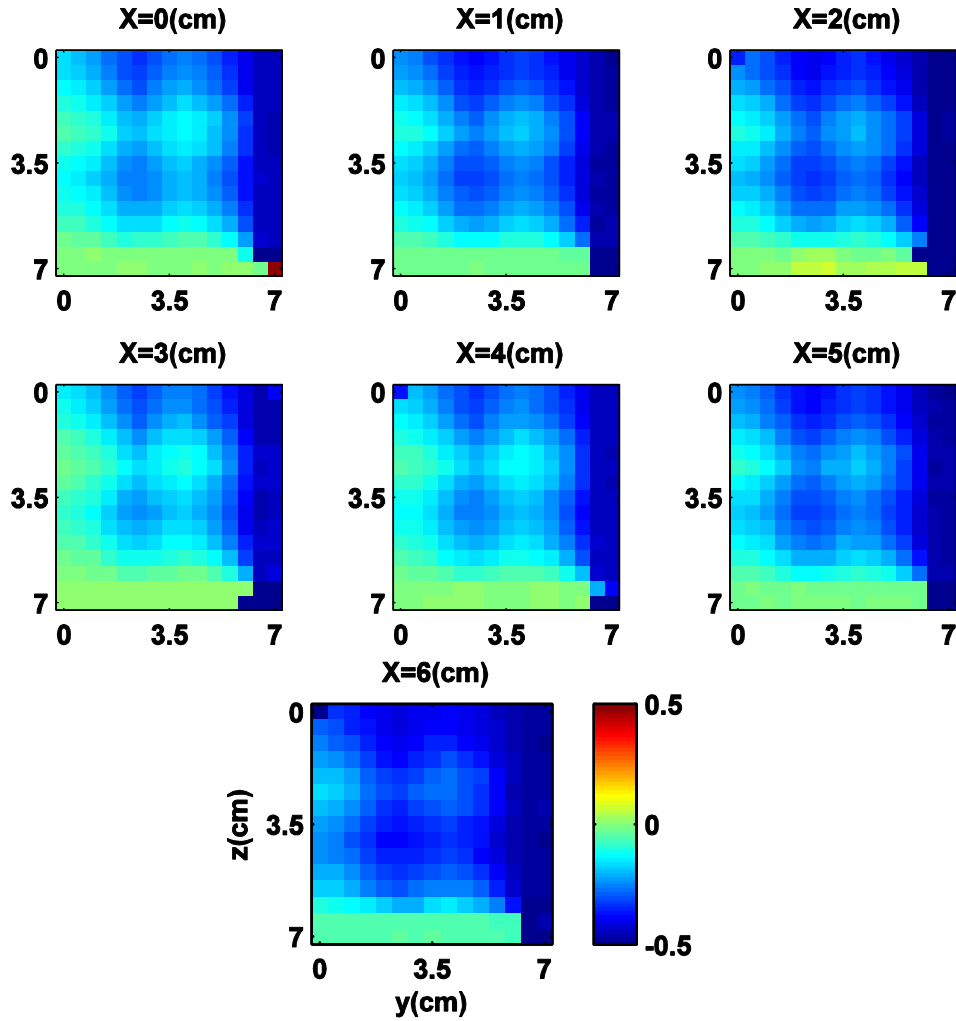


Figure 3.4: The error map of i-shift in x direction. The horizontal and vertical axes in each graph are y-axis (in cm) and z-axis (in cm). All units are in cm including the color bar. The error map shows the shrinking of tracked locations.

The regions with small error (light blue to green) are those regions in which the other pair of detector modules (Module #1 and #3) has higher detection angle. Since module #1 and #3 does not have misalignment and has good resolving power in the x-direction, they contribute more towards a better estimation of x coordinate. The results also show that, when the misalignment is on the x-direction, error in y and z components are almost zero.

3.4 Results of Misalignment in Y Direction

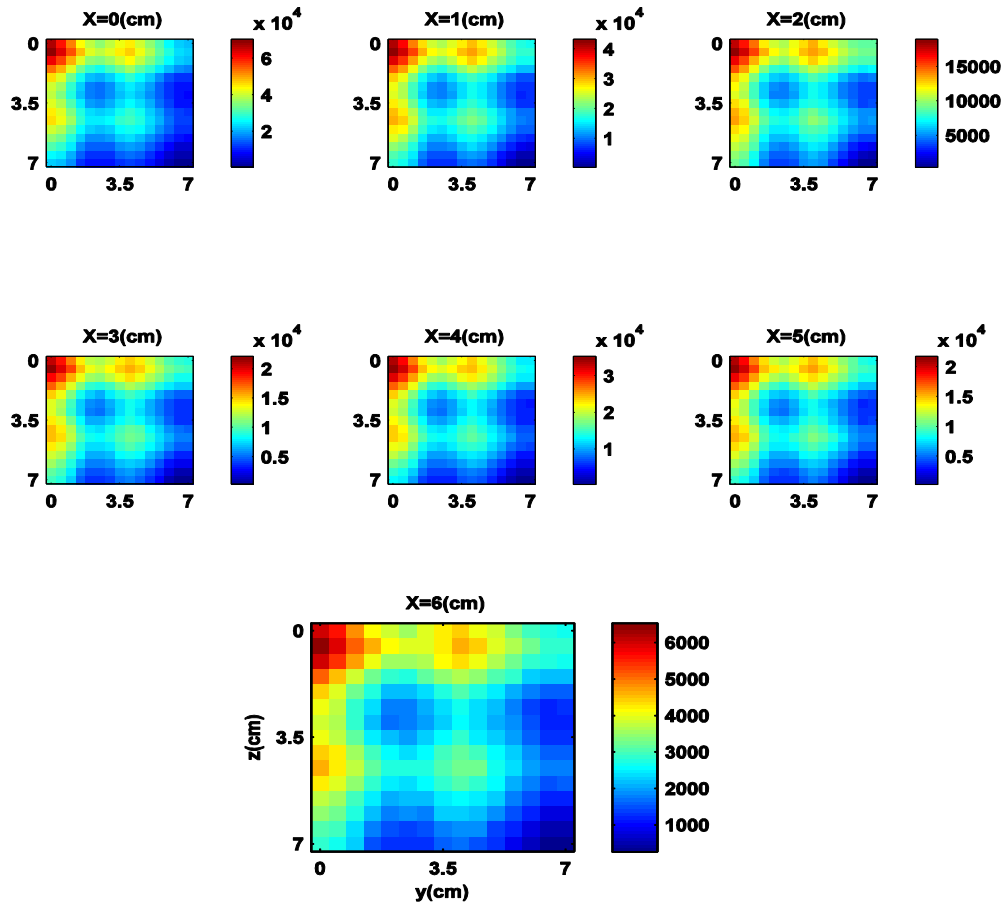


Figure 3.5: The sensitivity map of j-shift is shifted upward with respect to configuration B. The horizontal and vertical axes in each graph are y-axis (in cm) and z-axis (in cm).

Comparison between Figure 2.8 and the figure above shows that the sensitivity maps look almost the same, except that the sensitivity map in figure 3.5 has shifted downward along the z direction slightly.

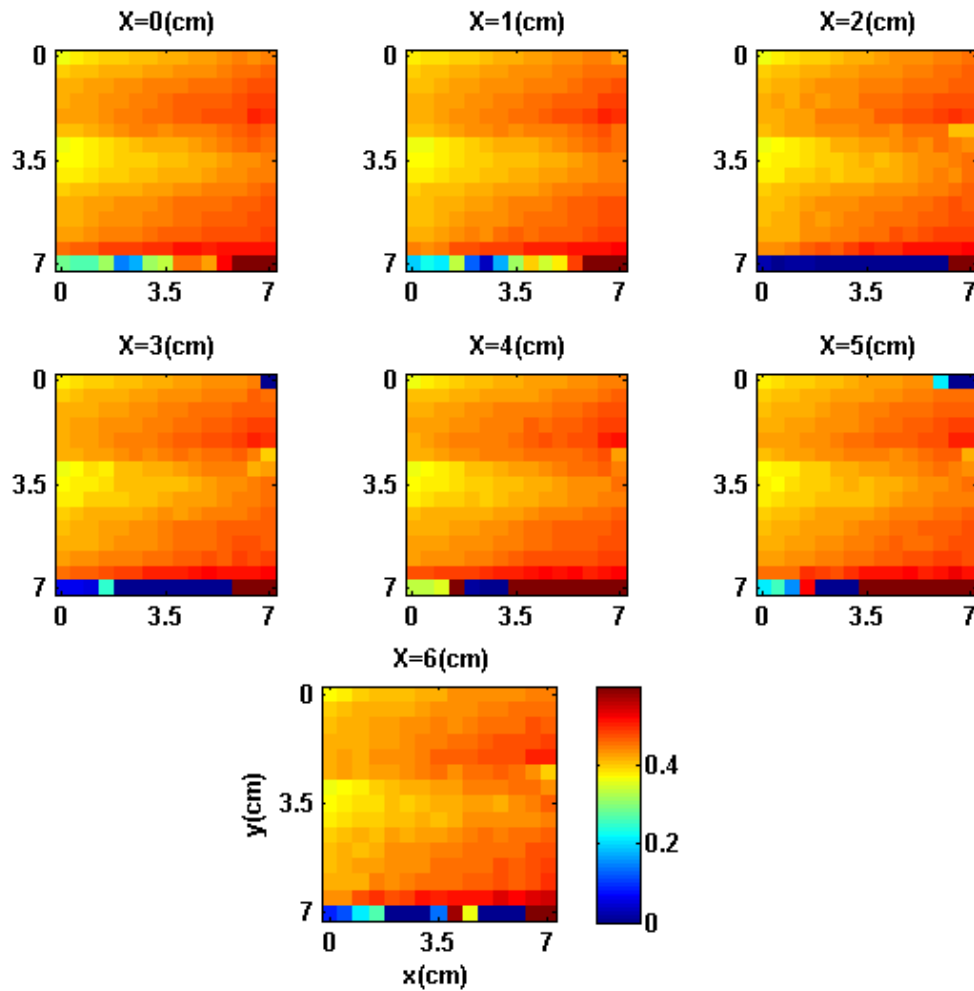


Figure 3.6: The error map of j-shift in y direction. The horizontal and vertical axes in each graph are y-axis (in cm) and z-axis (in cm). All units are in cm including the color bar.

Figure 3.7 shows a maximum error of 4 mm which is about half of the misalignment (8 mm) in y direction. The error in the x and z direction is zero, which is expected. The structure on the error map of Figure 3.6 is not observed in Figure 3.7, this is due to the fact, the good pair of detector modules (Module #1 and #3) has poor resolving power along y direction (Figure 3.3), and so they cannot help correcting the errors along y.

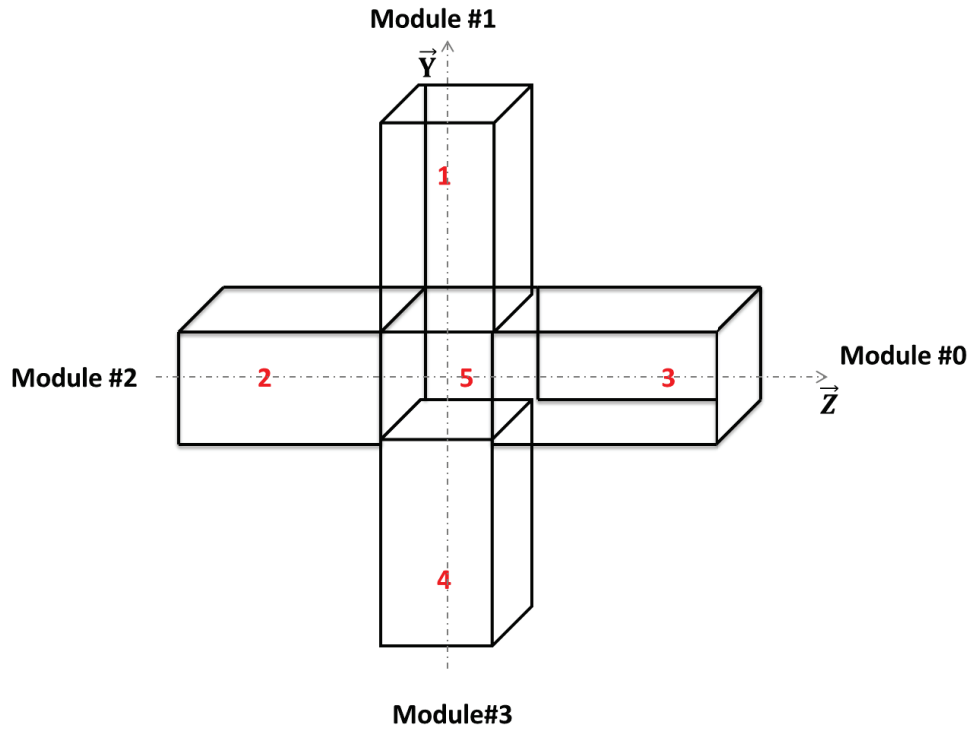


Figure 3.7: The FOV of detector modules along main axes.

3.5 Discussion

The effect of misalignment is evaluated on the detector configuration. The structure of the sensitivity maps changed slightly, consistent with the shifting of FOV when detector is shifted. The misalignment introduce an error of about half of the amplitude of misalignment. This is expected since the FOV is at the middle of detector pairs. It is found that the error only occurs in the direction of misalignment.

Chapter 4

Calibration of PeTrack System

4.1 Overview

It is essential to calibrate the PeTrack system in order to ensure a precise tracking. Simulations of PeTrack prototype clearly determine the boundary of the FOV. As revealed by simulations in chapter 2 and 3, PeTrack has a systematic distortion and possible distortion due to misalignment. The major systematic distortion is that tracked coordinates seems to have a smaller absolute value than the actual coordinates, as if there is a scaling factor from distortion, especially along the X-axis. In this chapter two experiments have been done to calibrate the scaling factors, a first order correction, of PeTrack on the x-z and x-y planes.

4.2 Set-up of the Calibration Experiment

Referring to chapter one Figure 1.9, the principle axes of PeTrack divides the 3D space by two planes: x-z and x-y. The first step in a calibration experiment is to select a grid phantom of which the distances between the grid points are precisely known. I chose the same grid that is used to

calibrate the x-ray C-arm distortion. The grid phantom consists of a matrix of 16×16 grid points, and the distance between the grid points is 1.40 cm. There are holes on grid point, on which the positron emission source Sodium 22 ($1.5 \mu\text{Ci}$) can be inserted with a source holder. The grid plane is mounted on a stand which is paralleled either to the x-y or x-z plane of PeTrack system and is exactly 45 degrees above from the horizon. Figure 4.1 and 4.2 display the alignment of all components in both x-y and x-z planes.

4.2.1 Calibration in Both Direction

The first step is to find the isocentre of PeTrack on the grid. I set the point source Sodium 22 on the center of the grid phantom. Then I adjusted the height of the stand and the position of the phantom while monitoring the source location with PeTrack system. Until the source location reaches a (x, y, z) location that is very close to the isocenter. Due to the limited adjustability of the stand, the closest we can achieve are (-0.03, -0.02, -1.12) cm for x-z plane calibration and (0.03, 0.22, -0.05) cm for x-y plane calibration. Then I fixed the phantom and the stand so that will not move during the experiment. After identifying the isocentre of PeTrack system, the boundary of FOV area could be ascertained. The goal was to study the possible shrinking or expansion distortion in the x, y, and z directions. I did measurements of source position at the middle of the FOV along the x, y, and z axis as well as on some boundary points and middle points. At every grid location 40-60 of measurements of 3D location of the source are recorded by the PeTrack.

These number of tracked data need to be averaged. Table 4.1 displays the grid data and the part of the tracked data for both planes in 3D.

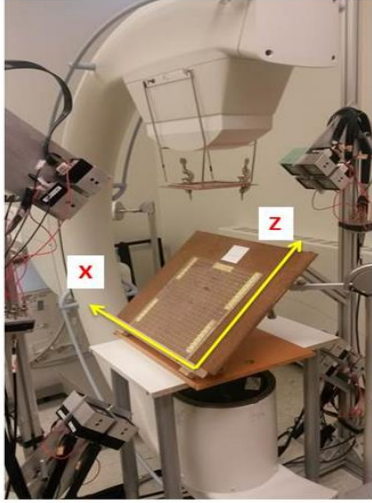


Figure 4.1: Calibration on X-Z plane

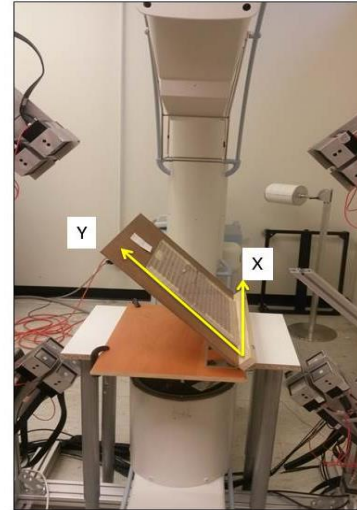


Figure 4.2: Calibration on X-Y plane

Table 4.1: Part of the calibration data on x-z and x-y plane.

I	J	K	X(cm)	Y(cm)	Z(cm)
4	0	0	5.39±0.04	-0.03±0.03	0.14±0.03
4	0	2	5.40±0.02	-0.05±0.03	3.03±0.04
4	0	-2	5.38±0.02	-0.04±0.03	-2.68±0.03
3	0	0	4.08±0.02	0.00±0.03	0.21±0.02
3	0	3	4.15±0.02	-0.03±0.02	4.38±0.02
3	0	-2	4.10±0.02	-0.033±0.02	-2.69±0.03
2	0	0	2.79±0.02	-0.04±0.03	0.20±0.02
4	-2	0	5.46±0.03	-2.59±0.04	-0.03±0.02
4	-4	0	5.43±0.03	-5.32±0.08	-0.05±0.02
3	0	0	4.19±0.02	0.20±0.02	-0.06±0.02
2	4	0	2.91±0.02	5.75±0.07	0.00±0.02
2	2	0	2.88±0.02	3.07±0.04	-0.05±0.02
2	0	0	2.88±0.02	0.22±0.03	-0.05±0.02
2	-2	0	2.84±0.03	-2.63±0.04	-0.04±0.02

4.3 Data Analysis

The table 4.1 shows both set of experimental data of two planes. The grid data represent the ideal location of the source on the grid. I, J, and K are indices of the grid point. For the grid points in x-y plane, the I, J are the index along x and y axis and the grid index K is set to 0. Similarly, for all the grid point on the x-z plan, the J index is set to 0. The grid phantom has a pitch of 1.40 cm

with accuracy of better than $\pm 0.005\text{cm}$. The goal of the calibration is to determine the actual PeTrack measurement of the pitch on the grid in 3D; i.e. dx , dy , and dz and then compare to the actual pitch of 1.40 cm . To obtain the mentioned pitches a fitting method should be applied to fit the PeTrack data (x, y, z) to the grid index (I, J, K) .

4.3.1 Calculations

Because the grid phantom was manually aligned to either the x-y or x-z plane of the PeTrack without precise alignment tools, it is expected there is some small translation and rotation between the grid phantom and the actual center x-y or x-z plane. The best mathematical tool to represent the rotation between two coordinate systems is a rotational matrix. The acquired data are in 3D therefore, a 3D rotational matrix is calculated, equation (4.1).

$$R = \begin{bmatrix} \cos \beta \cos \gamma & -\cos \beta \sin \gamma & \sin \beta \\ \sin \alpha \sin \beta \cos \gamma + \cos \alpha \sin \gamma & -\sin \alpha \sin \beta \sin \gamma + \cos \alpha \cos \gamma & -\sin \alpha \cos \beta \\ -\cos \alpha \sin \beta \cos \gamma + \sin \alpha \sin \gamma & \cos \alpha \sin \beta \sin \gamma + \sin \alpha \cos \gamma & \cos \alpha \cos \beta \end{bmatrix} \quad (4.1)$$

Equation (4.2) shows a transformation from grid indices to PeTrack coordinates, where x_0 , y_0 , and z_0 are the Translational constant and α , β , and γ are the rotational angles between the coordinate's axes. Parameters dx , dy , and dz are the PeTrack measured pitches along x, y, and z axes, respectively.

$$\begin{bmatrix} X \\ Y \\ Z \end{bmatrix} = [R] \begin{bmatrix} I \times dx \\ J \times dy \\ K \times dz \end{bmatrix} + \begin{bmatrix} x_0 \\ y_0 \\ z_0 \end{bmatrix} \quad (4.2)$$

Therefore there are 9 unknown parameters α , β , γ , dx , dy , dz , x_0 , y_0 , z_0 in the equation (4.2) and Origin Pro 9.0 software is used to fit the data for unknown parameters [22]. The list square fitting has been done for both planes using the data set listed in Table 4.2.

4.4 Results

The results of fitting parameters for pitches are:

Table 4.2: The results of the fitting for x-y and x-z planes		
$dx = 1.37 \text{ cm}$	$dy = 1.39 \text{ cm}$	$dz = 1.39 \text{ cm}$
$x = 0.04 \text{ cm}$	$y = 0.22 \text{ cm}$	$z = -0.014 \text{ cm}$
$x_1 = -0.04 \text{ cm}$	$y_1 = 0.004 \text{ cm}$	$z_1 = 0.20 \text{ cm}$
$\alpha = 0.001$	$\beta = 0.01$	$\gamma = 0.00$
$\alpha_1 = 0.00$	$\beta_1 = 0.01$	$\gamma_1 = -0.01$
Scaling Factor (x) = 1.022	Scaling Factor (y) = 1.007	Scaling Factor (z) = 1.007

The results of fitting are used to generate the true location of grid points rotated and translated coordinates in Cartesian coordinate. The scaling factors are calculated by dividing the value of true pitch by the fitted parameters dx , dy , and dz . Figure 4.3 illustrates the experimental and rotated data on x-z plane.

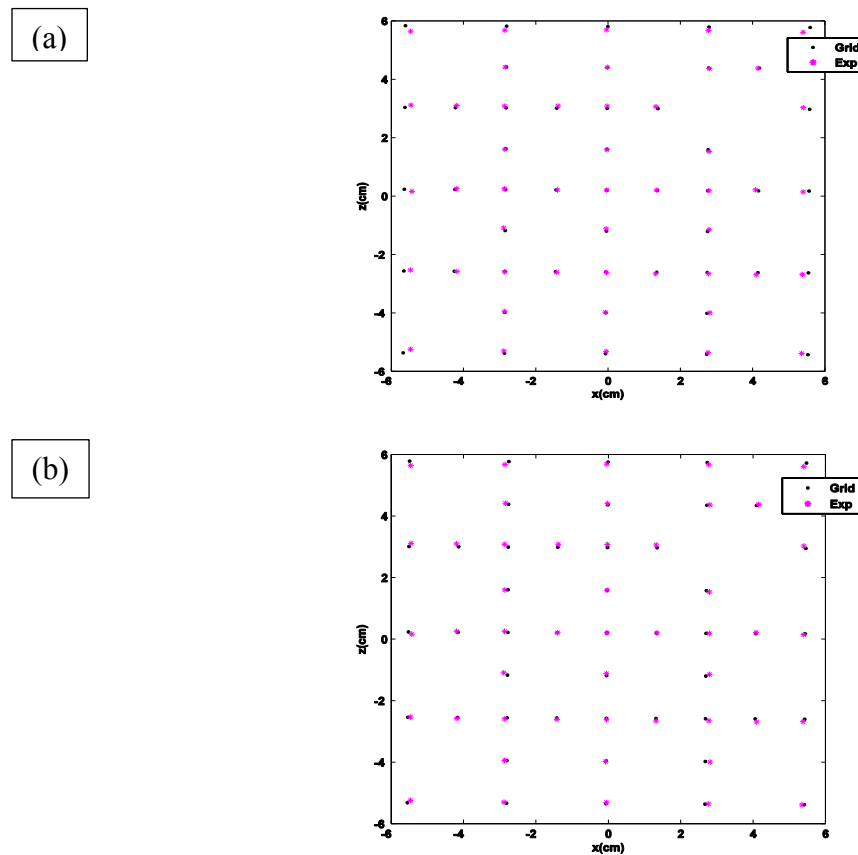


Figure 4.3: The result of experimental and true grid data on X-Z (a) Non-scaled data (b) Scaled data

The figure also compares the experimental data with grid data in two different cases with and without considering the scaling factor. According to the graphs, the measurements and true locations are in a good agreement at the centre of the plane. At the boundary of the FOV the discrepancy is increasing since only one pair of the detectors can receive the gamma rays from the annihilations. The figure also show overestimation (expanding) of experimental data around $x = \pm 3$. The expansion trend is consistent with Figure 2.15 in chapter 2.

Figure 4.4 illustrates the measurements and true locations on x-y plane and compares them by applying scaling factor and without scaling factor.

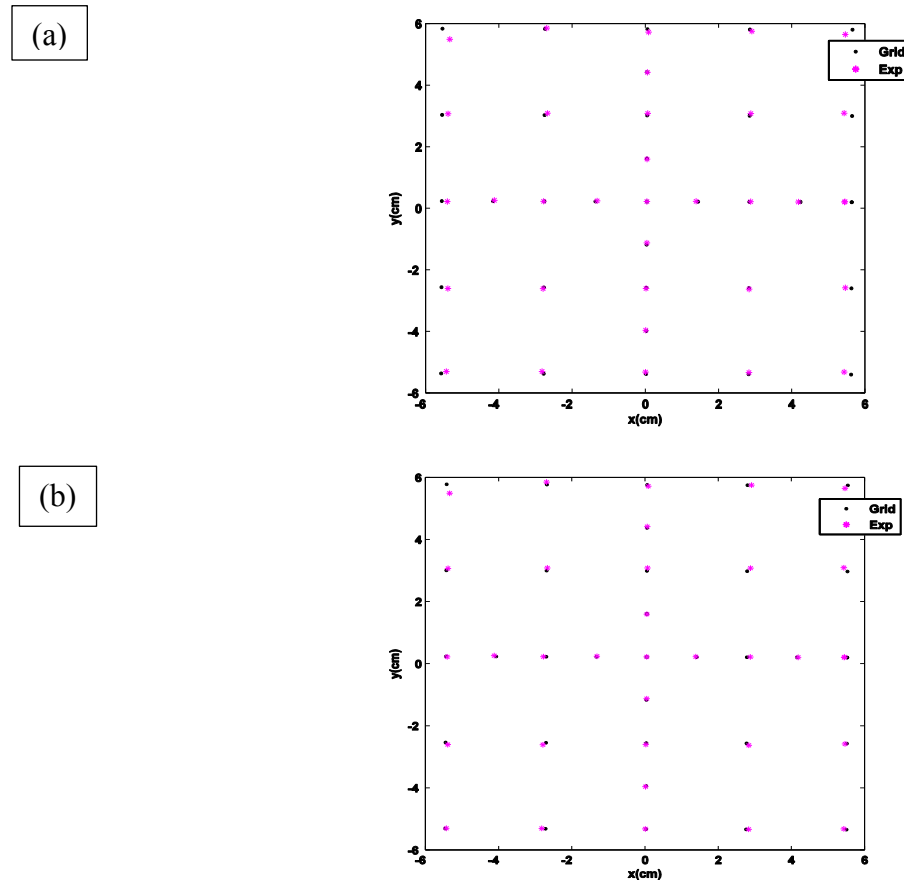


Figure 4.4: The result of experimental and grid data on X-Y (a) Non-scaled data (b) Scaled data

The trend of distortion is similar to Figure 4.3. In part (a) of both figures an expansion is observed at $x = \pm 3$ and applying the scaled factors enlarges the expansion as seen in part (b) of

the figures. In addition, the average deviation between experimental data and true locations is calculated for all the data applying the scaled factors and without scaled factors for both planes.

The results are shown in table 4.3.

plane	x-z	x-y
Average without scaled factors	$0.081 \pm 0.05(\text{cm})$	$0.104 \pm 0.09(\text{cm})$
Average applying scaled factors	$0.078 \pm 0.03(\text{cm})$	$0.078 \pm 0.05(\text{cm})$

4.5 Repeatability

A good tracking system should have good repeatability. Because the point source is positioned at each grid point manually, there could be some errors due to the positioning. Also, we would like to check the uncertainty of PeTrack measured 3D positions. Thus, we did the repeatability test for PeTrack by tracking the source in a few randomly selected locations on the grid phantom and repeating the test for some locations 3-4 times. Some of the repeatability test results are displayed in Table 4.4. The repeatability results showed consistency for the different measurements of a single location. The standard deviation is in the order of 0.01cm which reveals minimum fluctuations for the averaged data.

X (cm)	Y(cm)	Z(cm)
0.041 ± 0.009	0.218 ± 0.003	-0.01 ± 0.012
2.878 ± 0.002	0.215 ± 0.006	-0.046
-2.78 ± 0.009	0.23 ± 0.003	0.03 ± 0.026
-5.41 ± 0.003	0.225 ± 0.008	0.049 ± 0.005
0.05 ± 0.004	-5.324 ± 0.013	-0.032 ± 0.011
5.45 ± 0.009	0.21 ± 0.007	-0.1 ± 0.015

4.6 Discussion

PeTrack system was calibrated using a regular 2D grid. The calibration experiment proved that PeTrack is able to distinguish all the source positions across the FOV.

The calibration was accomplished by fitting the experimental data with the grid locations. The outcome of fitting leads us to the value of the dx, dy, and dz which respectively, show 2%, 1%, and 1% of underestimation compared to the true value of the pitch, corresponding to a scale factor of 0.98, 0.99, and 0.99 in the X, Y and Z directions, respectively. The experimental data show a general pattern for distortion across the FOV on both planes. At $x = \pm 3$ cm on both planes an expansion for the experimental data is observed. The expansion is in agreement with the simulation results of chapter 2, Figure 2.15 and confirms that PeTrack is locally distorted. The obtained scaled factors can improve the results to some extent. Since the scaled factors are compensating the general shrinking of PeTrack they are not useful for the correction of local expansion regions. The value of calculated average error after global scaling correction is less than 1 mm. If an error of better than 1 mm is required, it will need a local distortion correction. The maximum standard deviation in the repeatability test was 0.01 cm which confirms that PeTrack has sub-millimeter precision.

Chapter 5

Sensitivity and Distortion Survey of the Prototype PeTrack System

5.1 Overview

In chapter 4, the point source was manually placed at a set of different locations on a grid phantom. It did provide precise scale calibration of the PeTrack system; however, it is desirable to survey the FOV in finer steps. In this chapter, I set up two experiments on an x-y plotter that automatically moves the source throughout the FOV. The goal of the experiment is to survey the sensitivity and distortion of the prototype PeTrack and testing its ability to follow a moving source. Likewise the simulation studies in chapter 2 the source has a raster motion on both x-y and x-z planes. Moreover, the method of data analysis applied in this chapter is similar to the calibration method.

5.2 Instrumentation and Method

A 2D x-y plotter (Allen Data Graph), the calibration grid, and the 45-degree stand is used to perform this experiment. The x-y plotter has a pen cartridge that moves on the plotter surface to different positions according to analog voltage inputs V_x and V_y . A computer controls two-channel Digital to Analog Converter (ADC) (1208FS, Measurement Computing, USA) which is used to generate proper voltage signal to control the position of the pen cartridge. The ADC can be controlled using LabView software. One point ^{22}Na source is attached to the cartridge and is tracked by the PeTrack system. The activity of the source is $13.54 \mu\text{Ci}$. Firstly, the x-y plotter needs to be calibrated. A program is written in LabView to calibrate the voltage and the motion of the plotter pen cartridge such that its motion started and ended at pre-defined coordinates [20]. To perform the calibration, a piece of paper with printed 2D grid is taped on the surface of the plotter; the grid on the paper is designed using software and the pitches of the grid are exactly 1 cm in both directions. The x-y plotter is calibrated to move 1 cm per 250 mV along both directions of the plotter. During the calibration, the plotter shows a nonlinearity of about 1~2%. After the calibration two tracking experiments are performed in x-z and x-y plane. The sodium-22 source is placed on the plotter pen cartridge to be moved across the defined area. Figure 5.1 shows the experiment arrangement where the plotter is mounted on the stand which is along the x-z plane of PeTrack system (with y approximately equal to zero). Similar to the simulation, a raster motion is defined for the source using a code in LabView [20]. Also, knowing the boundary of the FOV from the simulation, the range of the raster scan is set to be (-5, 5) in the two scanning directions (Figure 5.2). The area of the scan therefore, is $10 \times 10 \text{ cm}^2$. The step size of the raster scan is set to be 1 cm in all directions. The source moves from one position to the next in a fraction of second, then the source stops 15 seconds at each location.

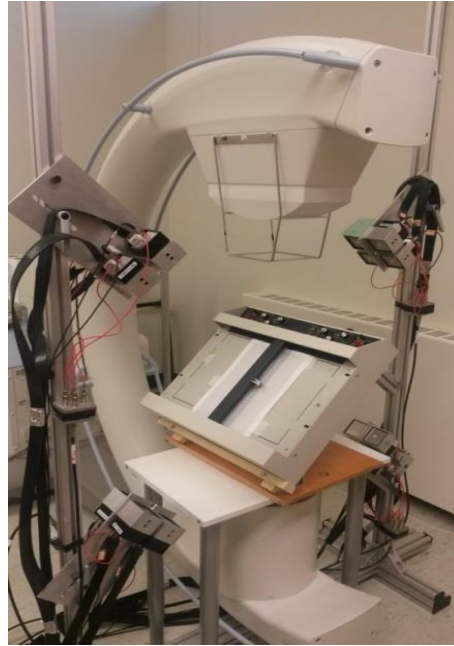


Figure 5.1: Tracking a moving source on x-y plotter

That gives PeTrack enough time to record enough data for each source location. Due to the intrinsic uncertainty of the tracking, the recorded locations are fluctuating around the true location. The 15 second pauses at each location allow at least 10 sets of localization data for each location (even for the points at the edge of the FOV). These data are then averaged to minimize the random fluctuation to determine if there is any distortion. The experiment is conducted for each of PeTrack's two planes. As in chapter 4, fitting is done to map the tracked locations by PeTrack to the expected true plotter positions using equations 4.1 and 4.2.

5.3 Results

PeTrack data is fit to the true locations of the source in order to obtain the 9 parameters including: rotation angles, translations, and the value of the pitches. The plotter step size between locations is 1 cm. The results of pitches are shown in table 5.1.

Table 5.1: PeTrack measured pitches in x-y plotter experiment

$$dx = 0.994 \text{ cm}$$

$$dy = 0.997 \text{ cm}$$

$$dz = 0.998 \text{ cm}$$

After applying the scaling factor derived from the above pitch result, both tracked and true

locations are shown in Figure 5.2.

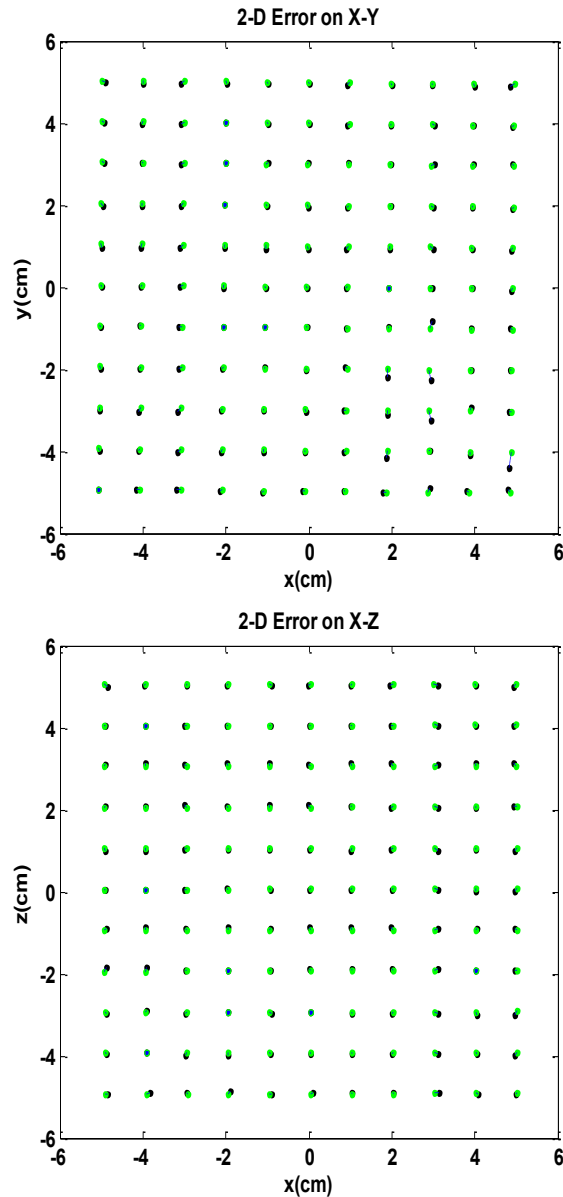


Figure 5.2: The tracked locations (blue) and true locations (green)

The above 2D scatter plot in x-y plane demonstrates the expansion of the tracked locations at $x = \pm 3$ cm while showing shrinking of tracked locations at the other areas including the edge of FOV. The trend remains the same for x-z plane.

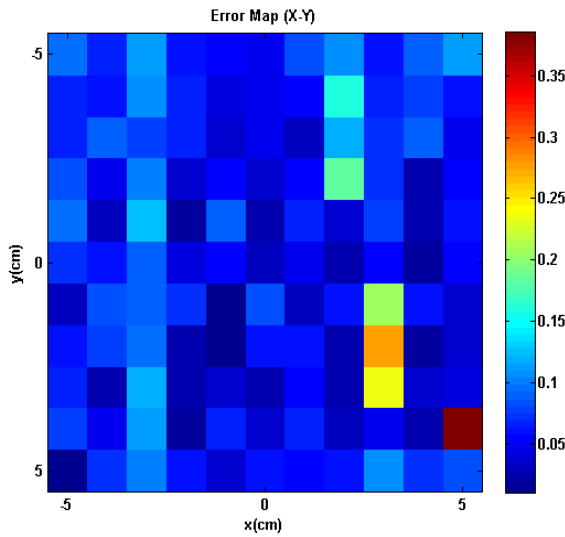


Figure 5.3: Deviation of tracked and true locations on x-y plane. All units are in cm including the color bars.

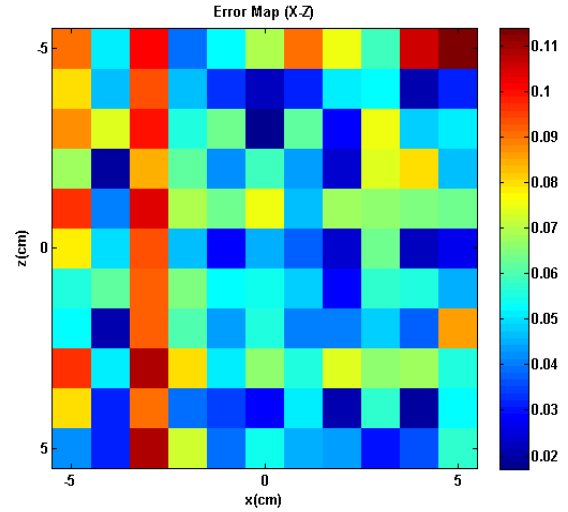


Figure 5.4: Deviation of tracked and true locations on x-z plane. All units are in cm including the color bars.

The maximum depicted error on the x-y plane is 4 mm which occurs at the edge of the FOV. The error in x-z plane is less than 1 mm across the FOV. The error plot of x-z plane remains relatively uniform in the FOV.

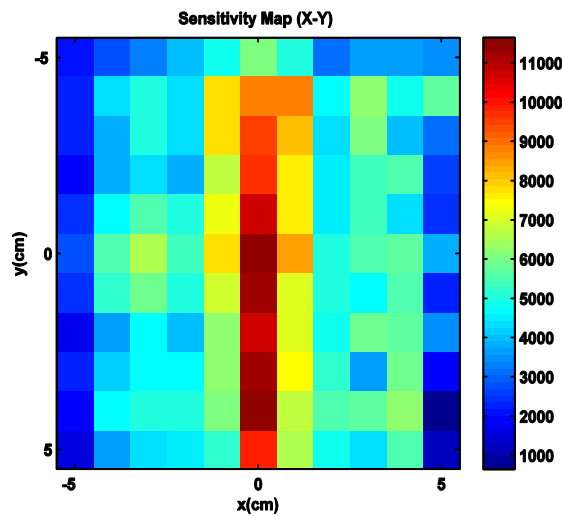


Figure 5.5: Sensitivity map on x-y. The sensitivity is represented by count/sec / (13.54 μ Ci).

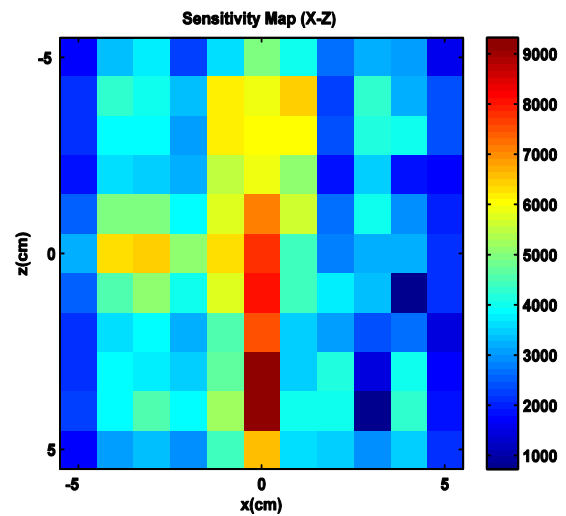


Figure 5.6: Sensitivity map on x-z. The sensitivity is represented by count/sec / (13.54 μ Ci).

The Figure 5.5 and 5.6 show the sensitivity map on x-y and x-z planes. The sensitivity maps of the detector for both planes show a similar trend. The detectors receive the maximum number of counts in the middle of the FOV. The number of counts decreases while approaching the edge of

the FOV. The maps also illustrate asymmetric distribution between left and right of the sensitivity map, especially on the x-z plane (Figure 5.6). In order to investigate this issue, x-ray image of the plotter is taken. The x-ray image demonstrates that most of the electronic and hardware components of the plotter, such as a transformer, are located at one side of the plotter. Therefore, gamma rays are attenuated by these electronic components and the number of counts drops significantly. In addition, in order to compare with the result of the simulations I plot the prototype PeTrack's simulation results for the x-y plane (Figure 5.7). Moreover, the difference in the sensitivity plots could also be the results of the non-identical PMTs used in the each detector module. The sensitivity map of simulation has the same trend and structure as experiment. Note that the activity of the source used for experiment is $13.54 \mu\text{Ci}$ and for the simulation is 1 mCi. Therefore, the absolute value is not directly comparable.

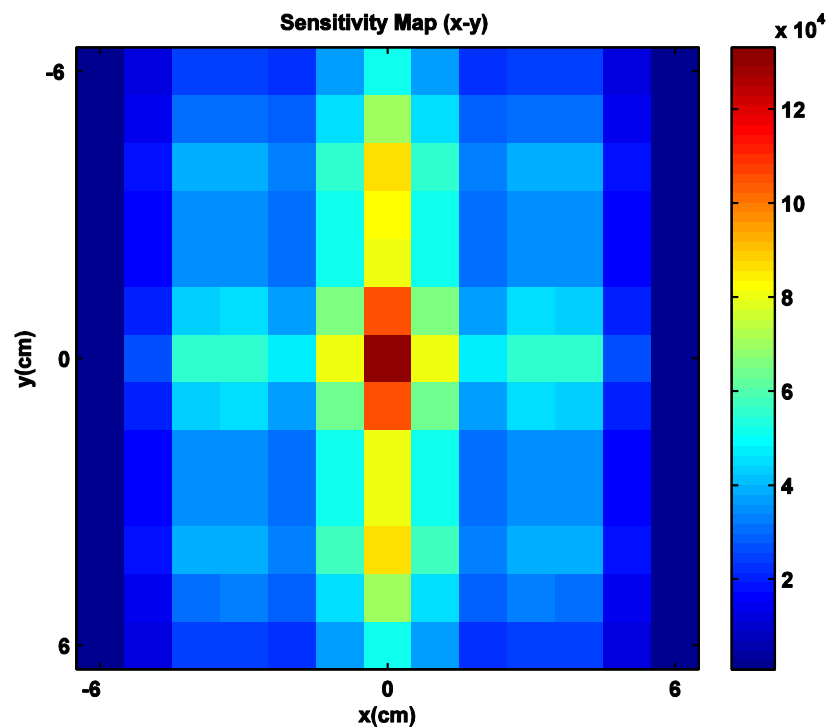


Figure 5.7: Sensitivity map of prototype simulation on x-y. The horizontal and vertical axes in each graph are x-axis and y-axis, respectively. The sensitivity is represented by count/sec/ (1 mCi).

5.4 Discussion

The fitting of the tracked locations to the ideal locations yield values of shrinkage of about 1% in all three directions. This shrinkage distortion is smaller than that obtained by grid phantom study in Chapter 4. This could be due to the observed non-linearity of the x-y plotter. Both error plots show an error no more than 2 mm within the FOV. The maximum error is reported in the edge of FOV which is expected due to the decreasing solid angle coverage. The error of less than 2 mm is comparable to the current tracking techniques used in surgical interventions [1, 24]. Therefore, the current accuracy of the PeTrack prototype is deemed to be acceptable.

Chapter 6

Integration of PeTrack with x-ray System

6.1 Overview

As mentioned in Chapter 1, one of the applications of PeTrack is to integrate with surgical x-ray system; therefore, real-time tracking of targets can be done without constant x-ray fluoroscopy. In this chapter, the PeTrack system is co-registered with x-ray surgical C-arm. Then, x-ray images are used as the road map and the PeTrack tracked target locations are indicated on the image to evaluate the performance of the integrated system. In chapter 4, the PeTrack scaled factors were obtained in 3D, which are applied in this chapter to improve the results of tracking.

6.2 Dual X-ray/ PeTrack Calibration Phantom

The Calibration phantom contains 6 steel balls (2.5 mm in diameter) for x-ray projection geometry calibration. It also has 4 positron-emitting point sources for PeTrack co-registration. The x-ray calibration balls are attached to the phantom by Aluminum tube along the x, y, and z

axis of the phantom reference frame at different distances from the center. A carbon fibre tube is used to secure the connection of steel ball to the phantom. Four positron sources are added to the x-ray phantom 4 mm from the top of 4 steel balls at $+x$, $+y$ and $\pm z$ axis. The positron sources are placed inside an acrylic housing. An additional aluminum tube is added to secure the positron sources to the phantom. Since the x-ray geometric calibration is very sensitive to the ball location, the x-ray phantom is machined precisely and the accuracy of the ball locations is within $\pm 50 \mu\text{m}$. Figure 6.1 displays the dual phantom [16].

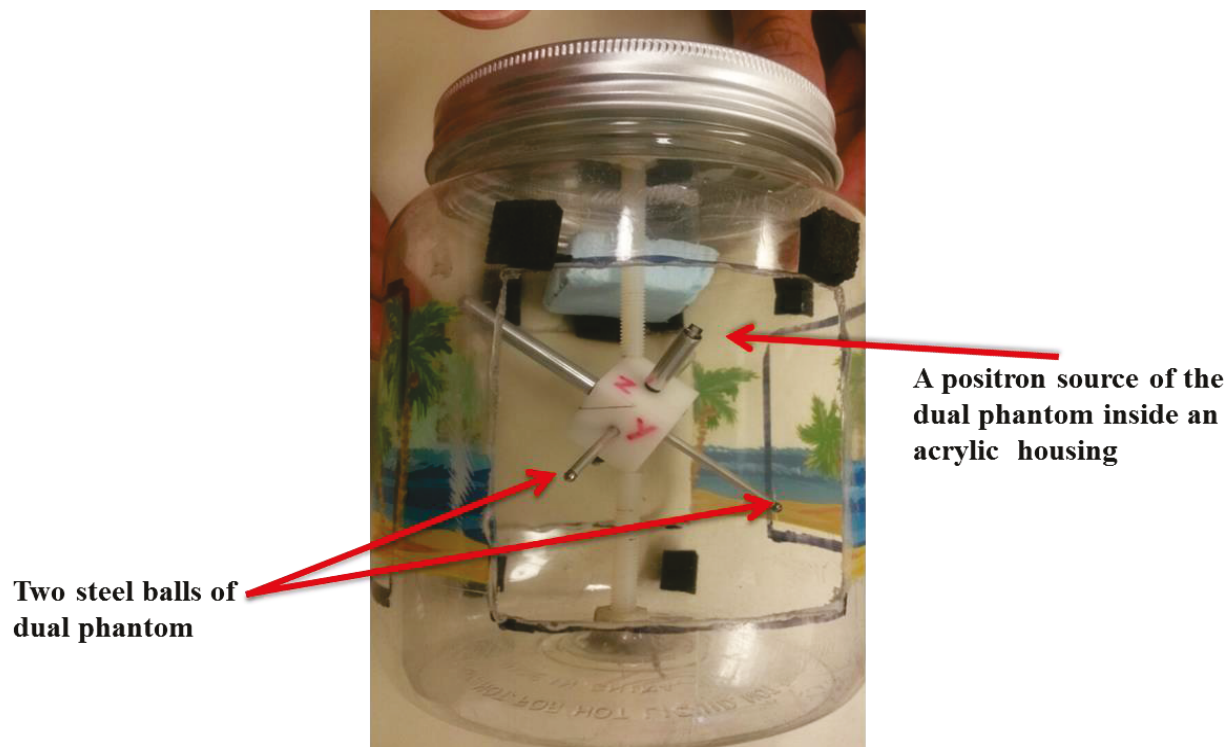


Figure 6.1: The dual phantom of PeTrack. It consists of 6 steel ball which are detectable by x-ray and four positron source which can be tracked by PeTrack. The positron source are placed on top of the steels balls. The figure shows two of the steel balls and one positron source which inside an acrylic housing.

6.3 Co-registration

The dual phantom described above is used to co-register x-ray C-arm and PeTrack. The dual phantom is placed in the middle of the common FOV of both systems. The projection images of

the dual phantom are acquired with the x-ray C-arm. In the meanwhile, PeTrack system localized the 4 positron emission markers on the phantom in the PeTrack coordinate frame. The x-ray images of the phantom are saved as raw images and corrected for x-ray image distortion [16]. The x-ray projection geometry can be calibrated by 9 parameters, which are the detector position, the detector orientation and the source position [16]. With these parameters, any point in the 3D reference frame of the dual phantom can be projected on the x-ray image. A projection point $(u(\vec{r}), v(\vec{r}))$ specifies how a 3D point \vec{r} can be projected onto the detector $(u(\vec{s}), v(\vec{s}))$ which is described by Equation 6.1.

$$u(r) = u_s + f \frac{(\vec{r} - \vec{s}) \cdot \hat{u}}{(\vec{r} - \vec{s}) \cdot \hat{n}} \quad v(r) = v_s + f \frac{(\vec{r} - \vec{s}) \cdot \hat{v}}{(\vec{r} - \vec{s}) \cdot \hat{n}} \quad (6.1)$$

Where f is the distance from the source to the detector, \vec{s} is the location of the source, and \hat{u} , \hat{v} , and \hat{n} are the unit vectors describing the detector orientation [16].

In dual phantom the sources are extended from four faces of the cube and their coordinates are: $(k_x, 0, 0)$, $(0, k_y, 0)$, $(0, 0, +k_z)$, $(0, 0, -k_z)$ where $k_x \neq k_y \neq \pm k_z$. The values for k would be measured relative to the centre of the phantom. The precise location of the four PeTrack sources in the phantom frame is known from the construction of the phantom (Table 6.1). The PeTrack also report their location in the reference frame of PeTrack system. The co-registration is done by finding the rotation and translation from PeTrack reference frame to the dual-phantom frame. Then, any PeTrack tracked location will be able to transform to the dual-phantom frame then be projected onto the x-ray image [16].

Table 6.1 displays the true locations of 4 positron source and also their tracked locations. The calculated deviation for both measurements shows that error of PeTrack system is about 0.2 mm.

Table 6.1: The original and tracked source locations on dual phantom. [16]			
K value	Original Length (mm)	PeTrack Measured Length (mm)	Deviation of Tracked and original Source Location (mm)
k_x	35.2 ± 0.1	35.14 ± 0.17	-0.06 ± 0.19
k_y	45.3 ± 0.1	45.5 ± 0.22	0.20 ± 0.24
$+k_z$	25.3 ± 0.1	25.6 ± 0.16	0.25 ± 0.19
$-k_z$	25.3 ± 0.1	25.6 ± 0.15	0.25 ± 0.18

Figure 6.2 shows an x-ray image of dual phantom which the tracked source locations are superimposed on the figure using ImageJ [23].

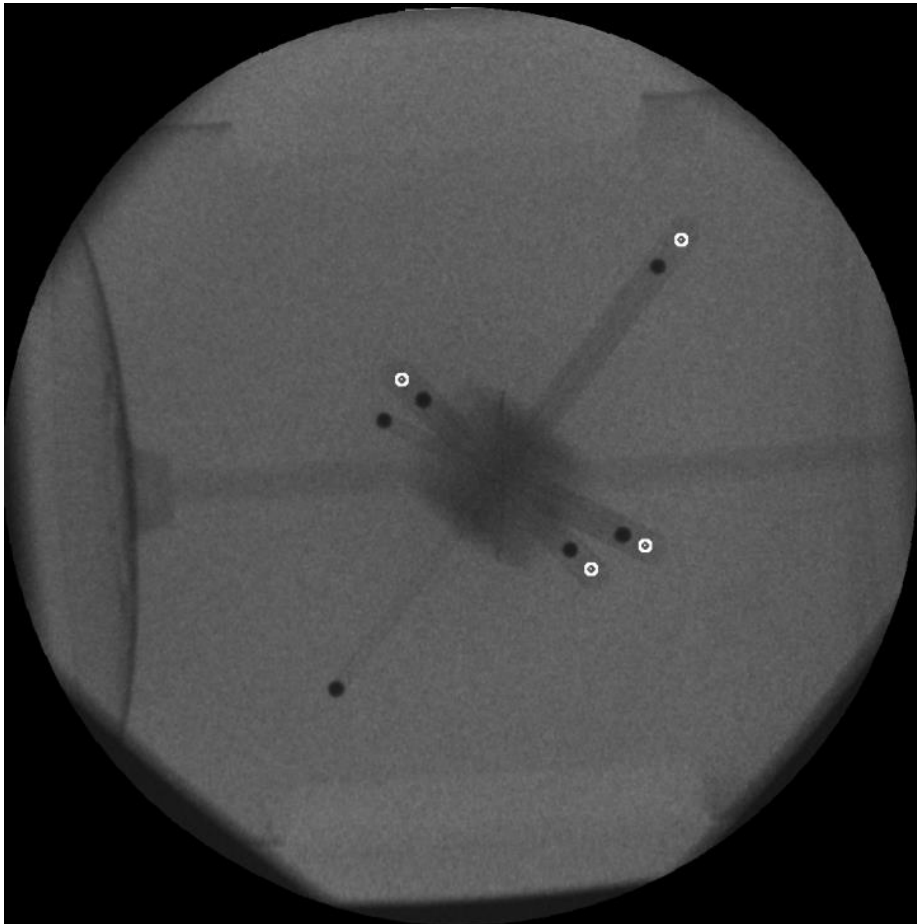


Figure 6.2: An x-ray image of dual phantom with source locations superimposed on it. The 4 white circles display the locations of positron sources tracked by PeTrack and the 6 black dots are the locations of the steel balls imaged by x-ray.

6.4 A Moving Source inside a Tube

This experiment is an application of PeTrack which tracks a source inside a tube, which models the movement of positron emission marker labeled catheter inside a blood vessel. The experiment is performed by moving the source inside a curved Aluminum tube. X-ray projections were acquired and source locations are tracked by PeTrack. The PeTrack locations are corrected using the scale factor obtained in Chapter 4. Then the source locations are transformed into dual-phantom frame and projected on to the x-ray image.

6.5 Results

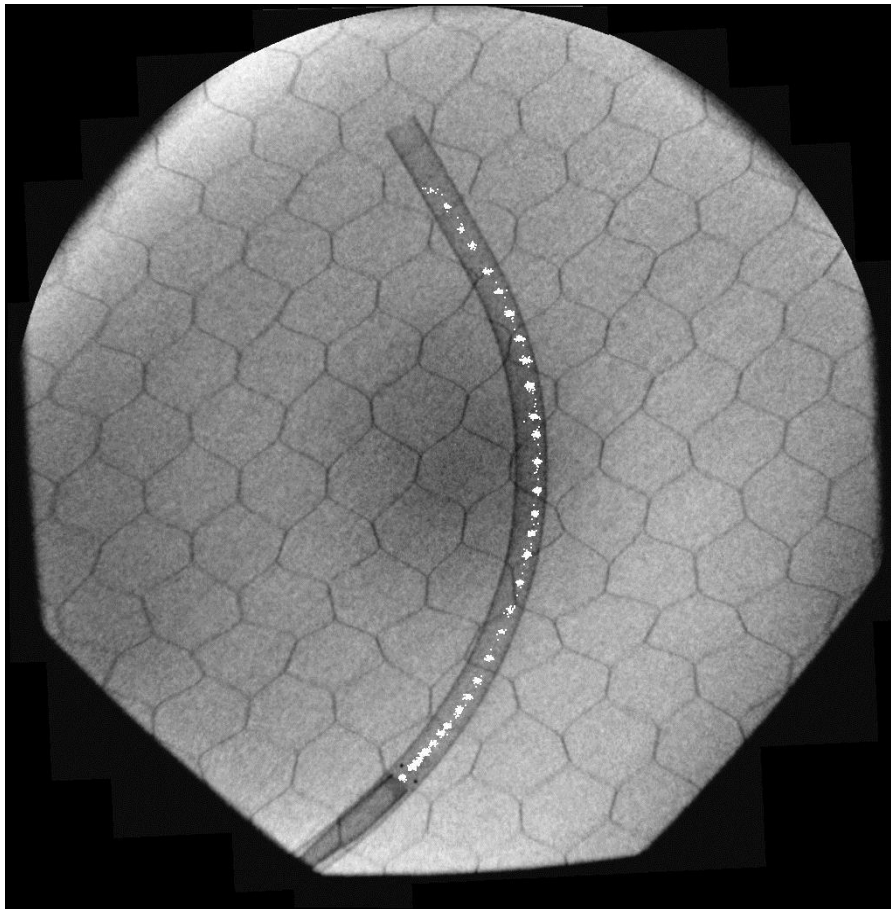


Figure 6.3: The image shows an application of PeTrack in tracking a positron source inside an Aluminum tube with diameter of 4 mm. The white points show the distribution of the tracked source locations in each move within the tube.

In Figure 6.3, the white dots show all of the scaled and tracked positron source locations which are superimposed on the figure without averaging using ImageJ [23]. They show the location of the source while it is moving inside the Aluminum tube. Figure 6.3 shows displacement for the two last tracked locations at the top end of the tube as the source getting out of FOV. Moreover, the source is moved inside the tube for 35 different locations however the obtained results show 34 points on the Figure 6.3. Therefore, we can conclude that PeTrack did not track the last location of the source which was completely outside of the FOV.

6.6 Discussion

The concept of co-registration is introduced. A tracking experiment was conducted. The tracked sources are scaled with the parameters which were obtained in chapter 4. The scaled tracked source locations show the true location of the source inside the tube and within the FOV. There is one missing tracked location which was outside of the FOV. Due to the distortion of the PeTrack system can be partially compensated by applying the global scaling factors. In this project the scaled parameters were applied to the experimental data and shows good tracking results.

Chapter 7

Conclusion & Future Work

7.1 Simulation Studies

The simulation studies revealed the boundaries of FOV in 3D. It also indicated the most effective configuration for the FOV, i.e. a detector with a bigger cross section will have a better coverage of the FOV. The simulation of the detector misalignment showed that the misalignment of the detector could introduce distortion to the PeTrack. Consequently, Monte Carlo simulation was proven to be useful on PeTrack detector design and configurations

7.2 Sensitivity

The sensitivity of the PeTrack for different configurations is studied. It is shown that the sensitivity is dependent on the geometry of PeTrack especially the arrangement of detector blocks. The study shows that increase the gaps between PeTrack detector blocks can enlarge the FOV. However, too large gap will cause low sensitivity regions or even blind spots inside the

FOV. For PeTrack detector modules with 4 detector blocks, it was found that the gap between the gaps should not be larger than the size of a detector block to avoid blind spots. The sensitivity plot was very helpful for evaluating PeTrack configurations.

7.3 Distortion

PeTrack system showed a non-uniform distortion across its FOV. The distortion is mostly observed at the edge of the FOV. However, the simulation and experiment results confirmed the some local expansion or shrinking distortion of the tracked position in some regions of FOV. In the present work the distortion is corrected with global scaling factors, and the tracking accuracy was improved to some extent (average residual error = 0.78 mm). If better tracking accuracy is required, local distortion correction method should be used.

7.4 Future Work

PeTrack is a prototype which is under development. It has the ability of tracking the source with accuracy of 1 mm. If better tracking accuracy is required, local distortion correction method should be used. Because of the 3D nature of the PeTrack, in order to correct the distortion within the 3D volume, we need to scan through a 3D grid to survey through the whole FOV. This can either be done experimentally with a xyz moving stage, or performed virtually using Monte Carlo simulation. This step can be taken in future to obtain more accurate tracking data from PeTrack.

Other future projects on PeTrack could be about either its hardware or software improvement. In terms of hardware, the PeTrack detector configuration can be altered under the guidance of Monte Carlo simulation method developed in this thesis. In the PeTrack software the tracking

code can be modified and integrated with distortion correction. The PeTrack can be integrated with Siemens x-ray c-arm system so that the tracking and display become real-time. All these steps can improve the reliability and efficiency of PeTrack as a real time tracking system.

References

- [1]. Y. Ma, "Real-Time x-Ray Fluoroscopy-based Catheter Detection and Tracking for Cardiac Electrophysiology Interventions," *J. Med. Physics*. **40** (7), (2013).
- [2]. M. Smuck *et al.*, "Duration of Fluoroscopic-Guided Spine Interventions and Radiation Exposure Is Increased in Overweight Patients," *J. American Academy of Physical Medicine and Rehabilitation*. **5**, 291-296, (2013).
- [3]. A. M. Franz *et al.*, "Electromagnetic Tracking in Medicine – a Review of Technology, Validation, and Applications," *J. IEEE Transactions on Medical Imaging*. (UnPublished).
- [4]. A. P. Shah *et al.*, "Expanding the Use of Real-Time Electromagnetic Tracking in Radiation Oncology," *J. Applied Clinical Medical Physics*. **12** (4), (2011).
- [5]. L. Brix *et al.*, "Three-dimensional Liver Motion Tracking Using Real-Time Two-Dimensional MRI," *J. Med. Physics*. **41**(4), (2014).
- [6]. A. Pesaveno *et al.* "New Real-Time Strain Imaging Concepts Using Diagnostic Ultrasound" *J. Med. Physics*. **45**, 1423-1435, (2000).
- [7]. T. Xu *et al.*, "Real-time tumour tracking using implanted positron emission markers: Concept and simulation study," *J. Med. Phys.* **33** (7), (2006).
- [8]. "MPET Readout System for Positron Sensitive PMTs, Coincidence Timing".

- [9]. H. E. Johns and J. R. Cunningham, *The Physics of Radiology*, 4th ed. (Springfield, Illinois, 1983), pp. 84-85.
- [10]. E. B. Podgorsak, *Radiation Physics for Medical Physicists*, (Springer, Berlin, Heidelberg, New York, 2005), pp. 159-160.
- [11]. J. C. Gonzalez *et al.*, “Positron Range Estimated with PeneloPET”, *J. Phys. Med. Bio.* **58**, (2013).
- [12]. S. R. Cherry and M. Dalhlbom, *PET: Physics, Instrumentation, and Scanners*, edited by M. E. Phelps (Springer, California, 2006), pp. 9-10.
- [13]. W. Drozdowski *et al.*, “Scintillation Yield of Bi₄Ge₃O₁₂ (BGO) pixel Crystals,” *J. Physica B.* **405**, 1647-1651, (2010).
- [14]. M. Soleimani, Msc thesis, Carleton University, 2009. pp. 14-17.
- [15]. M. Chamberland, Msc. thesis, Carleton University, 2009. pp. 9-11.
- [16]. B. A. Spencer, Msc. thesis, Carleton University, 2012.
- [17]. A. P. Hammersley *et al.*, “Calibration and Correction of Spatial Distortion in 2D Detector System,” *J. Nuclear Instrument and Methods in Physics Research A.* **346**, (1994).
- [18]. S. Jan *et al.*, “GATE: a simulation Toolkit for PET and SPECT,” *J. Phys. Med. Bio.* **49**, (2004).
- [19]. Computer Program ROOT Version 5.32.00,
- [20]. Computer Program LABVIEW, (National Instruments, 1998)
- [21]. Computer Program MATLAB, 2011.
- [22]. Computer Program Origin Pro 9.0, 2013.
- [23]. Computer Program IMAGEJ

[24]. N. Miyamoto *et al.* “A Motion-Compensated Image Filter for Low-Dose Fluoroscopy in a Real-time Tumour-Tracking Radiotherapy System” *J. Journal of Radiation Research*, **10**, 1-11, (2014).